Preprint cover page

This manuscript is a non-peer reviewed preprint submitted to EarthArXiv.
It has been submitted for publication in Atmospheric Pollution Research.

Meteorological associations of hourly $PM_{2.5}$ in Lhasa, Tibetan Plateau: antecedent weather, trend specification and out-of-sample evaluation

Zhongjie Ma[1]*

[1] Reading Academy, Nanjing University of Information Science & Technology, Nanjing 210044, China
*Corresponding author. Email: zhongjiema2023@outlook.com

ORCID: https://orcid.org/0009-0007-6050-8083

Licence: CC BY 4.0

Meteorological associations of hourly $PM_{2.5}$ in Lhasa, Tibetan Plateau: antecedent weather, trend specification and out-of-sample evaluation

Zhongjie Ma[1]*

[1] Reading Academy, Nanjing University of Information Science & Technology, Nanjing 210044, China

*Corresponding Author. Email: zhongjiema2023@outlook.com

Abstract: Statistical models that relate $PM_{2.5}$ to meteorology are widely used to separate weather from emission effects, but they are rarely evaluated out of sample in clean, high-altitude cities, and the role of their trend term is seldom examined. This study fitted penalized additive spline models to hourly city-average $PM_{2.5}$ in Lhasa, Tibetan Plateau (about 3,650 m a.s.l.), for 2019–2024 (51,955 valid hours), using ERA5 temperature, relative humidity, wind speed and precipitation as current-hour and 24-hour antecedent predictors with seasonal, diurnal and long-term controls, and benchmarked them against calendar, linear and random forest models. Three results emerge. First, the point-estimated wind and humidity responses are carried mainly by antecedent conditions: in perturbation decompositions, the 24-hour terms carry most of the fitted wind and humidity sensitivity. Second, the trend specification governs both the weather-normalized series and out-of-sample bias: a linear trend forces a near-monotonic normalized decline (10.98 to 9.66 μg/m³), although observed annual means fell from 12.16 to 8.55 μg/m³ by 2022 and rebounded to 10.36 μg/m³ in 2024. Third, a model frozen after 2019–2024 explained 42% of hourly and 60% of daily variance in 2025 (RMSE 5.35 and 2.80 μg/m³; calendar-only benchmark: 32% and 41%) and modestly outperformed the linear benchmark, but errors were concentrated in winter and in a few high-concentration hours; Gutor-evening residuals exceeded the same-year, same-hour winter background in five of the six years of the 2019–2024 record. Weather-normalized trends for Plateau cities should therefore be reported with alternative trend specifications and event-level diagnostics.

Keywords: $PM_{2.5}$; Lhasa; Tibetan Plateau; weather normalization; generalized additive model; out-of-sample evaluation

1 Introduction

Temperature, relative humidity, wind speed and precipitation regulate $PM_{2.5}$ formation, dispersion and removal, with associations that vary across temporal scales and regional conditions (Jacob and Winner, 2009). Statistical models that relate concentrations to weather are therefore widely used to separate meteorological from emission-related variability (Grange et al., 2018; Vu et al., 2019), but their results depend on how temporal structure, and long-term change in particular, is represented. Hourly associations, interannual meteorological variability and long-term climate forcing (IPCC,

2021) require separate interpretation; short-term concentration changes alone do not identify a causal climate-change contribution.

Relationships between $PM_{2.5}$ and meteorological variables are commonly nonlinear. Wind affects pollutant dispersion and transport, while precipitation scavenging depends on intensity and antecedent accumulation. Relative humidity is associated with hygroscopic growth and secondary formation, and temperature influences partitioning, chemical reactions and atmospheric mixing. These variables covary, and their statistical relationships exhibit substantial regional variation (Jacob and Winner, 2009; Tai et al., 2010). Analysis for Lhasa consequently requires estimation of individual associations conditional on meteorological covariation and temporal structure, together with assessment of their stability.

Lhasa occupies a valley on the Tibetan Plateau, where regional background and local anthropogenic emissions jointly influence particulate concentrations. Duo et al. reported seasonal differences in meteorological associations, and Yin et al. identified urban–suburban contrasts and interannual variation (Duo et al., 2018; Yin et al., 2019). Chen et al. (2022) showed that uncertainty in local anthropogenic emission inventories can substantially affect simulated pollutant concentrations; local urban emissions dominate primary trace gases such as NOx and CO in Lhasa (Ran et al., 2014), and vehicular emissions of volatile organic compounds on the Plateau may be underestimated in current inventories (Huang et al., 2025). These findings indicate that interpretation of urban observations in Lhasa requires consideration of emission activity, valley dispersion and spatial representativeness rather than inference from regional background concentrations alone.

Simple correlation analysis cannot readily distinguish meteorological covariation, nonlinear responses and periodic temporal structure. Random partitioning of adjacent hourly records may also overestimate temporal generalization (Roberts et al., 2017). The 2018 standards amendment changed particle monitoring conditions, with national and local network transition schedules involving September 2018 and January 2019 (Ministry of Ecology and Environment, 2018). The present analysis covers 2019–2024 to reduce the influence of that transition on temporal comparability. Network changes, missing observations and grid representativeness at high elevation remain sources of uncertainty.

Random-forest weather normalization has already been applied to Plateau cities including Lhasa (Chen et al., 2023; Zhang et al., 2023). Zhang et al. (2023) included Unix time as a predictor representing the long-term emission trend. Previous work has examined whether temporal variables are resampled during weather normalization (Zheng et al., 2023). This study examines the specification of the fitted long-term term and its implications for normalized trends and subsequent-year bias; how this specification shapes the normalized series, and how such models perform on an independent year, have received little attention for high-altitude cities.

Using hourly city $PM_{2.5}$ observations and ERA5 reanalysis for 2019–2024 (Hersbach et al., 2020), this study applies a penalized additive spline model to estimate conditional associations with temperature, relative humidity, wind speed and precipitation while controlling seasonal, diurnal and long-term variation (Eilers and Marx, 1996). Benchmarks and expanding-window checks assess fit and generalization, while normalization and controlled perturbations characterize interannual variation and sensitivity (Grange et al., 2018; Vu et al., 2019). Frozen-model evaluation against 2025 observations tests transfer. This study addresses three questions: (1) are short-term associations carried by current-hour or 24-hour antecedent conditions; (2) how does the trend specification shape the normalized series and out-of-sample bias; and (3) how well does a model frozen after 2019–2024 reproduce 2025, and where are its errors concentrated?

2 Methodology

2.1 Study area and data

The study period runs from 1 January 2019 to 31 December 2024. The target variable is the hourly city-average $PM_{2.5}$ mass concentration obtained from the QuotSoft archive of real-time releases by the China National Environmental Monitoring Centre. Records labeled PM2.5 are retrieved from the Lhasa column in μg/m³; PM2.5_24h records are excluded. Missing concentrations are not interpolated. The spatial representativeness of the city average depends on the monitoring network and may change with its composition.

Meteorological inputs are ERA5 reanalysis data retrieved through Open-Meteo (Hersbach et al., 2020, 2023; Open-Meteo, 2023, 2026). The request specified models=era5, timezone=Asia/Shanghai, cell_selection=nearest, elevation=nan and wind_speed_unit=ms. The nearest grid cell is therefore selected, automatic elevation adjustment is disabled, and wind speed is expressed in m/s. For the requested location of 29.6667°N, 91.1333°E, the returned cell is at 29.7500°N, 91.2500°E with an elevation of 4233 m (Figure S2). It represents regional grid meteorology rather than conditions at an urban station. The 24 meteorological records for 31 December 2018 supply the antecedent predictors needed at the beginning of the analysis; they contribute neither response observations nor fitting samples.

2.2 Time units and quality control

The study period follows the official monitoring-state transition schedule (Ministry of Ecology and Environment, 2018). Concentrations retain their released units without an additional standard-to-ambient volume conversion, and no indicator for the 2018 reporting transition is included. Restricting the study period reduces comparisons across reporting states but does not remove potential temporal inconsistency arising from network or instrument changes.

2.3 Meteorological predictors

Let C_t denote $PM_{2.5}$ concentration and T_t, H_t, U_t and P_t denote temperature, relative humidity, wind speed and precipitation. With C_0=1 μg/m³ and P_0=1 mm, concentrations and precipitation are transformed as $\ln(1+C_t/C_0)$ and $\ln(1+P_t/P_0)$, retaining zero values and reducing right skewness. The model also includes a wet-hour indicator $I(P_t>0)$, preceding 24-hour means of temperature, humidity and wind, and cumulative precipitation. Lagged $PM_{2.5}$ concentrations are not included.

Antecedent predictors are calculated on the complete hourly axis over t−24 to t−1, excluding the current hour and future information. A missing required antecedent record invalidates the corresponding window variable. Hours with valid responses and all predictors are then selected, preventing concentration gaps from changing the window length. The 24-hour window represents persistence at the daily scale rather than a common physical causal lag, and previous-day precipitation has been identified as an important predictor of particulate trends in mid-latitude settings (Barmpadimos et al., 2011).

$$z_t = ln(1 + \frac{C_t}{C_0}) \quad (1)$$

$$a_{T,t} = \frac{1}{24}\sum_{\ell=1}^{24} T_{t-\ell} \quad (2)$$

$$a_{P,t} = ln(1 + \frac{\sum_{\ell=1}^{24} P_{t-\ell}}{P_0}) \quad (3)$$

2.4 Penalized additive spline model

A penalized additive spline regression is fitted on the log-concentration scale (Eilers and Marx, 1996). Functions f_j and g_j represent conditional associations for the four instantaneous and four antecedent predictors. Temporal controls c_t comprise an intercept, annual and diurnal cycles, weekday effects and a linear time trend. Annual and diurnal cycles each use three sine–cosine pairs, with annual phase calculated using the actual year length. The time trend is referenced to 1 January 2019. These terms control periodic and long-term temporal variation.

Each meteorological term uses cubic B-splines with six uniformly spaced knots and eight basis functions, centered on the training-sample mean. A second-difference coefficient penalty constrains curvature, and squared residuals are normalized by sample size. A numerical ridge of 10^{-8} is applied to non-intercept coefficients. The design matrix has 85 columns, and effective degrees of freedom are obtained from the penalized smoother trace. Because the eight centered B-spline columns of each term sum to zero, adding a common constant to a term's coefficients leaves both the fitted function and the second-difference penalty unchanged. This redundancy is a property of the parameterization only: the numerical ridge selects the minimum-norm coefficients, and the fitted functions, predictions and bootstrap intervals are numerically identical to those obtained under a conventional sum-to-zero constraint. The single penalty parameter is selected by temporal extrapolation error (Section 3.5), and the reported per-term effective degrees of freedom show that the fitted smoothness still differs among terms. Knots, centering parameters and coefficients are estimated within each training window; inputs beyond its boundaries receive linear extension.

The smoothing parameter λ is selected from six decade-spaced candidates between 10^{-6} and 10^{-1}. Expanding windows train from 2019 through the preceding year and evaluate 2021, 2022, 2023 and 2024, respectively. Selection minimizes mean original-scale hourly RMSE across the four evaluation years. The final model is then estimated using all valid 2019–2024 hours. Duan's smearing factor restores the original concentration scale (Duan, 1983), with negative predictions truncated to zero.

$$z_t = c_t + \sum_{j=1}^{4} f_j(x_{j,t}) + \sum_{j=1}^{4} g_j(a_{j,t}) + \beta_w I(P_t > 0) + \varepsilon_t \quad (4)$$

$$c_t = \alpha + s_{annual}(d_t) + s_{hour}(h_t) + \gamma_{weekday(t)} + \beta_\tau \tau_t \quad (5)$$

$$L(\theta) = \frac{1}{n}\sum_{t=1}^{n}(z_t - \eta_t)^2 + \lambda \sum_{j=1}^{8} \|D_2\theta_j\|^2 \quad (6)$$

$$\hat{C}_t = C_0 max\{0, S\, exp(\hat{\eta}_t) - 1\}, \quad S = \frac{1}{n}\sum_{t=1}^{n} exp(r_t) \quad (7)$$

2.5 Benchmark models and internal temporal evaluation

Benchmarks comprise a calendar model containing only temporal controls, a linear model using the same meteorological predictors, and a random forest (Grange et al., 2018). The forest uses 200 trees, a feature-sampling fraction of 0.8, a minimum leaf size of 60 and a maximum depth of 16; these settings were fixed in advance and were not tuned on 2025 data. All models use the same valid samples and temporal partitions. Performance is evaluated on the original concentration scale using hourly and daily root mean square error (RMSE), mean absolute error (MAE), mean bias error (MBE) and R^2. Daily metrics use observed and predicted means over identical paired hours. R^2 is referenced to the observed mean of the corresponding evaluation sample. Because the internal temporal checks also select λ, their reported performance may be optimistic relative to a fully independent evaluation. The random forest is trained on the original concentration scale, and pooled internal R^2 is referenced to the mean observed concentration of the pooled internal evaluation sample.

$$RMSE = \sqrt{\frac{1}{n}\sum_{t=1}^{n}(\hat{C}_t - C_t)^2},\ MAE = \frac{1}{n}\sum_{t=1}^{n}|\hat{C}_t - C_t| \quad (8)$$

2.6 Meteorological normalization and perturbations

Meteorological normalization estimates concentrations under a common reference weather distribution (Grange et al., 2018; Vu et al., 2019). Instantaneous and antecedent meteorological vectors are resampled within month–hour strata from the 2019–2024 reference period, with 200 draws per stratum. Temporal controls are retained at the target timestamps, and predictions are averaged on the original concentration scale. Annual observed and normalized means are calculated over the same valid hours. Interpretation remains dependent on the temporal-control structure, omitted emission variability and other unmodeled factors. Each draw is a randomly selected hour from the corresponding month–hour stratum of the reference period, and the 200 predictions are averaged for every target hour, so the number of draws is a fixed resampling resolution rather than a separate tuning parameter.

The complete 2024 meteorological series is perturbed separately by +1°C in temperature, +5 percentage points in relative humidity, and +10% in wind speed or precipitation. Antecedent predictors are recalculated, while other meteorological variables and fitted coefficients remain fixed. Relative humidity is capped at 100%; zero wind or precipitation values remain zero under proportional perturbations. Mean concentration changes are calculated over hours whose predictor values remain within the training marginal ranges both before and after perturbation. These calculations characterize local model sensitivity. The effects are decomposed into instantaneous and antecedent contributions in Section 3.4; these contributions are obtained by averaging their marginal contributions over the two possible perturbation orders (a symmetric two-group Shapley decomposition) on the concentration scale, and the two contributions sum exactly to the total change before rounding. Perturbing one variable at a time does not ensure consistency with the joint meteorological distribution or physical covariation. Because a 10% change in a small wet-hour accumulation is often below the 0.1 mm reporting precision, the precipitation perturbation is best read as a model elasticity rather than an observable concentration change.

$$\hat{C}_{t,norm} = \frac{1}{B}\sum_{b=1}^{B} h[\hat{m}(c_t, W_{r_b})] \quad (9)$$

$$\Delta C_s = \frac{1}{n_s}\sum_{t\in A_s}[\hat{C}(W_{t,s}) - \hat{C}(W_t)] \quad (10)$$

2.7 Uncertainty and sensitivity analysis

A sensitivity analysis excludes the highest 1% of concentrations to assess the stability of the conditional curves. Statistical analyses and numerical verification were run in environment A (Python 3.13.5; NumPy 2.1.3, pandas 2.2.3, SciPy 1.15.3, scikit-learn 1.6.1) with a base random seed of 20261013. The historical model-fitting environment (environment B: Python 3.12.14, NumPy 2.3.5, pandas 3.0.1, SciPy 1.18.1, scikit-learn 1.9.1) is recorded for provenance only. The frozen model state was rebuilt in environment A from the archived spline state, and the coefficient arrays are reused without refitting: the 7- and 30-day arrays were retained from the historical analysis archive, whereas the 14-day array was generated in environment A. Stage-specific seeds, retained artifacts and environment assignments are listed in Table S12. The author designed the study, collected and processed the data, selected the methods and formulas, carried out the original analyses and wrote the first draft. Analysis code was developed and modified with an AI coding assistant (DeepSeek-V4.1-Flash1017), and AI chat assistants, including ChatGPT (OpenAI), were used to review the analysis

and manuscript and to suggest revisions, which the author evaluated before adopting; the author is responsible for the code and results. Emissions, boundary-layer conditions and directional transport are not represented in the primary model (supplementary diagnostics are described in Section 2.9), and regional grid meteorology is used to interpret city-aggregate concentrations. Mechanistic interpretation is consequently limited by omitted variables and the difference in spatial scale between the meteorological inputs and the concentration observations (Chen et al., 2022; Jacob and Winner, 2009).

2.8 Independent evaluation with public data for 2025

Public data from 1 January to 31 December 2025 are used for temporal evaluation. $PM_{2.5}$ is obtained from the QuotSoft city archive of China National Environmental Monitoring Centre releases, retaining hourly PM2.5 values from the Lhasa column and the same response definition as the fitting period (QuotSoft, 2026). Meteorological inputs use the same ERA5 reanalysis source (Hersbach et al., 2020, 2023; Open-Meteo, 2026). The requested location is 29.6667°N, 91.1333°E; the returned grid cell is 29.75°N, 91.25°E at 4233 m, matching training, with elevation adjustment disabled. Evaluation concerns city-aggregate concentration and regional grid meteorology rather than observations at a specific central-city air or weather station.

Timestamps are expressed in China Standard Time, UTC+8, using the units and quality control in Section 2.2; shifting the meteorology by ±1 h changes the 2025 hourly RMSE by at most 0.023 μg/m³ (Table S10). Same-grid meteorology for 31 December 2024 supplies the strictly preceding 24-hour predictors; that day contributes neither validation concentrations nor additional fitting samples. Missing concentrations are neither interpolated nor replaced by zero. Daily evaluation requires at least 18 valid paired hours and calculates observed and predicted means over identical hours.

Spline knots, centering parameters, coefficients, λ and the retransformation factor from 2019–2024 remain fixed, as do the benchmarks; 2025 concentrations do not enter fitting or tuning. Models are evaluated on identical paired samples with hourly and daily RMSE, MAE, MBE and R^2, seasonal errors and the share outside training marginal ranges. Besides the primary frozen model, three variants were evaluated: trend frozen at 31 December 2024, trend removed with refitting, and year fixed effects replacing the linear trend, with the 2024 effect carried forward to 2025. The primary model and the three benchmarks were fixed before the 2025 data were examined; the three variants and the seasonal retransformation factor in Section 3.7 were added afterwards and are reported as exploratory diagnostics.

This test assesses retrospective estimation in a subsequent year using a consistent meteorological source. It does not assess advance weather forecasting or input from the National Basic Meteorological Station. Station observations have not entered this evaluation; measurement heights, averaging windows and data-scale changes require a separate future test (Hersbach et al., 2020; Roberts et al., 2017).

2.9 Supplementary diagnostics

In-sample residuals of the primary model are averaged within festival and control windows (dates in Table S1): Gutor evenings (20:00–24:00 on the Gutor date, i.e. the 20:00, 21:00, 22:00 and 23:00 labels of that date plus 00:00 of the following day, five hourly labels), the Losar window (day −2 00:00 to day +2 23:00), the Spring Festival window (from the listed Chinese New Year's Eve date at 00:00 through 23:00 two calendar days after that eve date, 72 hourly labels before exclusions), the 2020 national control period (24 January–31 March 2020) and the 2022 Lhasa static-management period (8 August–20 September 2022). Festival windows are made mutually exclusive (Gutor evening first; the Losar window excludes the Gutor night of 18:00–06:00; the Spring Festival window

excludes hours shared with Losar and Gutor), whereas the control periods may overlap the festival windows. Festival-window means are compared with a same-year, same-hour festival-excluded winter background (December–February hours outside all festival windows; control-period hours are retained in the background), with 95% intervals from resampling days within each window (events for the Gutor evenings). Control-period residuals are reported separately and, where indicated, are compared with the corresponding year-wide mean residual. Winter residuals are stratified by ERA5 boundary-layer-height quintile and 10 m wind sector, and a sensitivity model adds boundary-layer height, with both versions refitted on the hours that have boundary-layer data (Table S11); residuals by boundary-layer-height quintile and wind sector are reported in Tables S2 and S3. Nested models with temporal controls only, or with current-hour weather, antecedent weather or both, are compared on identical hours (Table S7). Interval robustness is examined with 7-, 14- and 30-day blocks (Table S8). A partial ERA5-Land check replaces ERA5 2 m temperature and relative humidity with ERA5-Land values for the nearest 0.1° cell (29.70°N, 91.10°E; 4,176 m) retrieved for 2013–2025 and used for 2019–2025, recomputes the 24-hour antecedent means, and refits the model with new knots and centering parameters and a re-estimated retransformation factor (Table S9).

3 Results

3.1 Coverage and concentration distribution

The 2019–2024 calendar period contains 52,608 hours, of which 51,955 (98.76%) have valid $PM_{2.5}$ concentrations and complete meteorological predictors. The 653 missing concentration hours are not interpolated. The city archive contains 2,191 daily files, with one calendar day missing; ERA5 meteorology is complete over the analysis period. Each monthly mean meets the requirement of at least 75% hourly coverage. Annual coverage is shown in Figure 1 and Table 1.

The mean, median and 95th percentile values of $PM_{2.5}$ are 10.42, 8.00 and 24.00 μg/m³ respectively and the maximum hourly value is 311 μg/m³. The annual means tend to decrease from 12.16 μg/m³ in 2019 to 8.55 μg/m³ in 2022 before increasing again to 10.36 μg/m³ in 2024 indicating nonmonotonic interannual variation. The observations here include the overall development of the city series and do not account for meteorological or emission contributions.

The single maximum of 311 μg/m³ occurred at 22:00 CST on 19 February 2023, during a short winter episode in which concentrations rose from 56 μg/m³ at 21:00 to 311 μg/m³ and decayed over the following hours. The episode coincided with very dry air (relative humidity 4–7%), weak wind (about 1 m s^{-1}) and no precipitation, conditions consistent with stagnant accumulation; the available observations cannot distinguish a dust intrusion, an instrumental spike and an emission episode. The peak coincided with the evening of Gutor, two days before the 2023 Tibetan New Year (Losar, 21 February), when torches are traditionally carried in the evening (China Tibet Online, 2023). Combustion associated with this ritual under very dry, stagnant conditions is therefore a plausible contributor, although the present data cannot confirm it; festival burning of butter lamps has been reported to raise Lhasa $PM_{2.5}$ to 240 ± 30 μg/m³ (Li et al., 2019). Night-time boundary layers in Lhasa are shallow, so evening emissions can be concentrated in a thin layer (Ran et al., 2022).

A residual analysis of festival and control windows is consistent with this interpretation, although the excess is dominated by 2023. Relative to same-year winter hours at the same clock times, Gutor-evening residuals are higher by +5.3, +2.6, +19.0, +8.1, +140.2 and −0.4 μg/m³ in 2019–2024 (positive in five of six years; two-sided sign test $p = 0.22$); the hour-weighted mean excess is +30.0 μg/m³ (95% event-bootstrap CI +3.1 to +76.6; +7.0 excluding 2023), and the equal-weight mean across years is +29.1 μg/m³ (+6.9 excluding 2023). Excluding the Gutor night that falls on day −2 of the Losar window, the Losar window residual is +2.9 μg/m³, +2.0 μg/m³ above its same-hour background (+0.4 to +3.9); the Spring Festival window, after removing hours shared with Losar and

Gutor, is −1.5 μg/m³, −2.4 μg/m³ relative to its same-hour background (−4.5 to +0.1). The 2020 national control period has a residual of −1.60 μg/m³, 2.5 μg/m³ below that year's mean, whereas the 2022 static-management residual (−1.86 μg/m³) is close to the year-wide bias (−1.61 μg/m³); after removing the year mean, only −0.24 μg/m³ remains, so the window-specific 2022 signal is small. Excluding 8 August–20 September 2022 raises the 2022 annual mean from 8.55 to 9.03 μg/m³ (9.29 μg/m³ if the window is extended to 21 October 2022). The four largest residual hours all belong to the 2023 Gutor night, and the ten largest fall on five calendar days dominated by that night and the following Losar period.

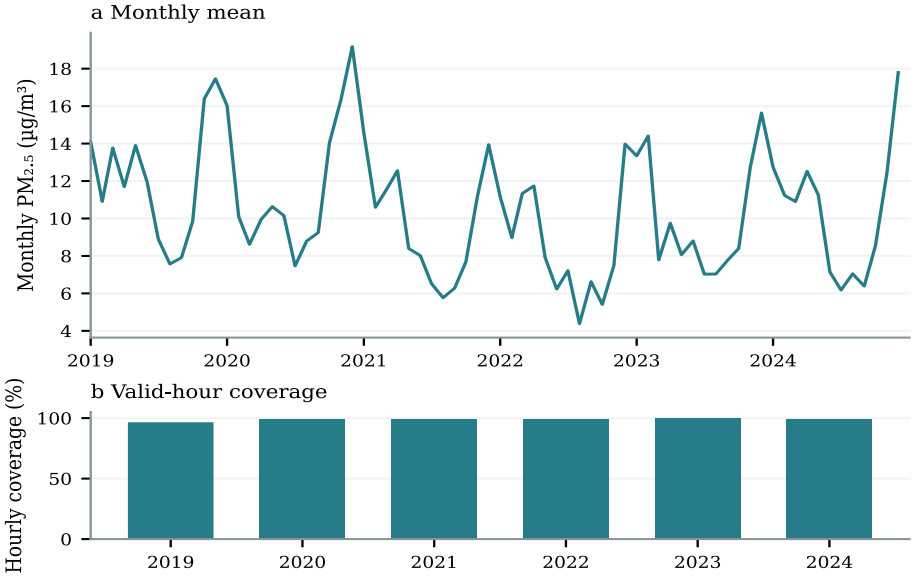


Figure 1: Monthly mean $PM_{2.5}$ concentrations and annual valid-hour coverage during 2019–2024. Monthly means require 75% of expected hours; annual coverage is referenced to complete calendar-year hours

Table 1: Annual $PM_{2.5}$ observation coverage and concentration statistics for 2019–2024

Year	Expected hours	Valid hours	Coverage %	Annual mean	95th percentile
2019	8,760	8,460	96.58	12.16	26.00
2020	8,784	8,725	99.33	11.71	27.00
2021	8,760	8,689	99.19	9.75	22.60
2022	8,760	8,693	99.24	8.55	20.00
2023	8,760	8,708	99.41	10.01	23.00
2024	8,784	8,680	98.82	10.36	24.00

Concentrations are in μg/m³; statistics use valid observation hours within each year. Annual means are computed over valid hourly values, and percentiles use linear interpolation between order statistics, so the 2021 95th percentile (22.60) is not an observed integer.

3.2 Seasonal and diurnal variation

$PM_{2.5}$ exhibits clear seasonal and diurnal variation (Figure 2). Seasons are defined as DJF (December, January and February pooled within each labeled calendar year), MAM, JJA and SON; winter has the highest mean at 13.74 µg/m³ and summer the lowest at 7.55 µg/m³. The observed diurnal cycle has a late-evening maximum of 15.62 µg/m³ at 22:00 CST and an early-morning minimum of 7.10 µg/m³ at 07:00 CST, with a secondary afternoon low of 7.77–8.05 µg/m³ at 16:00–17:00 CST and a second peak of 13.86 µg/m³ at 10:00. All hours in Figure 2 are expressed in China Standard Time (UTC+8). The model reproduces the main cycle structure, but both meteorological predictors and temporal controls contribute to the fit; agreement with these cycles does not independently establish the explanatory contribution of meteorology.

The seasonal cycle is broadly consistent with earlier observations in Lhasa (Duo et al., 2018; Yin et al., 2019). The diurnal timing is more site-dependent: several Chinese-city studies report an afternoon minimum and an evening-to-morning high, whereas this six-year city-average record places the minimum in the early morning (07:00) with a nearly equal afternoon low and the maximum late at night (22:00). Valley circulation, the seasonal mix of the pooled hours, and network averaging can all contribute; boundary-layer depth over the Plateau varies strongly between day and night (Che and Zhao, 2021; Ran et al., 2022), but this study does not separate these influences. Dispersion, precipitation scavenging and anthropogenic activity may contribute to these patterns. Emissions and boundary-layer processes are not directly observed in this study, so these mechanisms remain possible interpretations rather than explanations independently tested by the present data.

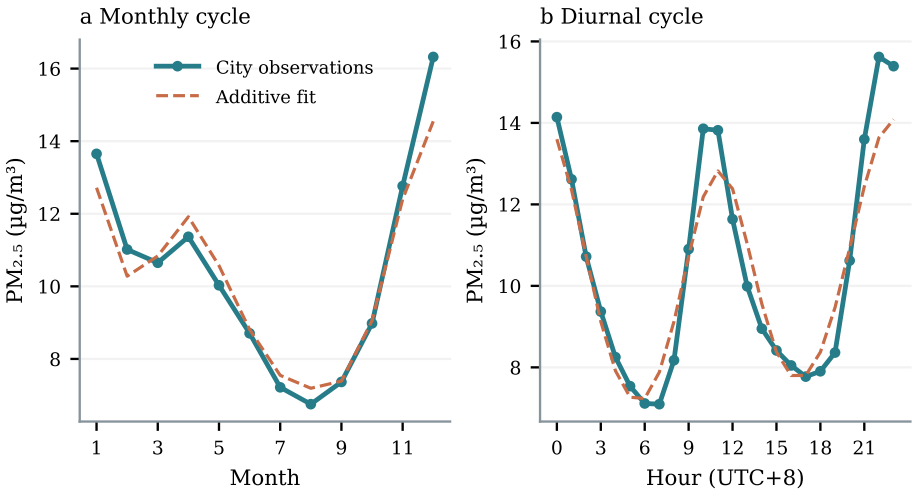


Figure 2: Monthly and diurnal $PM_{2.5}$ cycles in China Standard Time. Solid lines denote observations and dashed lines additive-model fits over identical valid hours

3.3 Instantaneous conditional associations

After conditioning on other instantaneous predictors, antecedent weather and temporal structure, the four variables exhibit distinct association patterns (Figure 3). Increasing temperature, relative humidity and wind speed from their 10th to 90th percentiles gives relative changes in C+1 of −0.5% (−9.10 to 15.80°C; 1,000-replicate seven-day block interval −13.8% to 14.0%), 5.5% (20.00% to 83.00%; −2.7% to 13.7%) and −0.2% (0.60 to 2.22 m/s; −2.8% to 2.0%), respectively. Increasing positive precipitation from its wet-hour 25th percentile of 0.10 mm to its 75th percentile of 0.40 mm gives a relative change of −5.9% (1,000-replicate seven-day block interval −8.4% to −3.6%).

The temperature, humidity and wind percentile-contrast intervals include zero, so their point estimates do not establish stable instantaneous directions. The positive-precipitation interval lies entirely below zero, indicating a negative statistical association under the specified controls. These findings concern the defined percentile contrasts and do not imply uniform responses across the full predictor ranges.

Conditional curves represent model multipliers on the C+1 scale and are not equivalent to percentage changes in concentration or predictor contribution fractions. The wet-hour indicator distinguishes dry from wet conditions, while partitioning instantaneous and antecedent terms depends on model specification. Sensitivity curves excluding the highest 1% of concentrations assess dependence on high values. These associations do not independently identify formation, transport or removal mechanisms (Tai et al., 2010; Zhai et al., 2019).

Three diagnostics qualify these contrasts. First, each instantaneous predictor is strongly correlated with its 24-hour mean (temperature r = 0.89; humidity 0.66; wind 0.55; log precipitation 0.46), so instantaneous and antecedent terms show substantial concurvity and their separate contributions are imprecise. Second, temporal controls alone explain 84% of the variance of instantaneous temperature and its 24-hour mean, 46% for humidity and 11–14% for wind and precipitation, so the temperature spline is identified from a small residual range. Third, pooled 10th–90th percentile contrasts span conditions rarely realized within the same month and hour: within the 288 month–hour strata, changes in C+1 are +2.1% (−3.0 to +7.1) for temperature, +4.9% (−0.8 to +10.3) for humidity and +1.4% (−0.7 to +3.3) for wind, with within-stratum spans 36%, 69% and 95% of pooled spans. The pooled contrasts therefore partly reflect seasonal and diurnal co-variation.

Excluding the highest 1% of fitting concentrations (507 hours; threshold 39 $\mu g/m^3$) changes the instantaneous temperature contrast from −0.5% to −2.2%, the humidity contrast from +5.5% to +5.2%, the wind contrast from −0.2% to −0.3% and the positive-precipitation contrast from −5.9% to −5.7%. The extreme values therefore influence the temperature contrast but not the sign or the approximate width of the other contrasts.

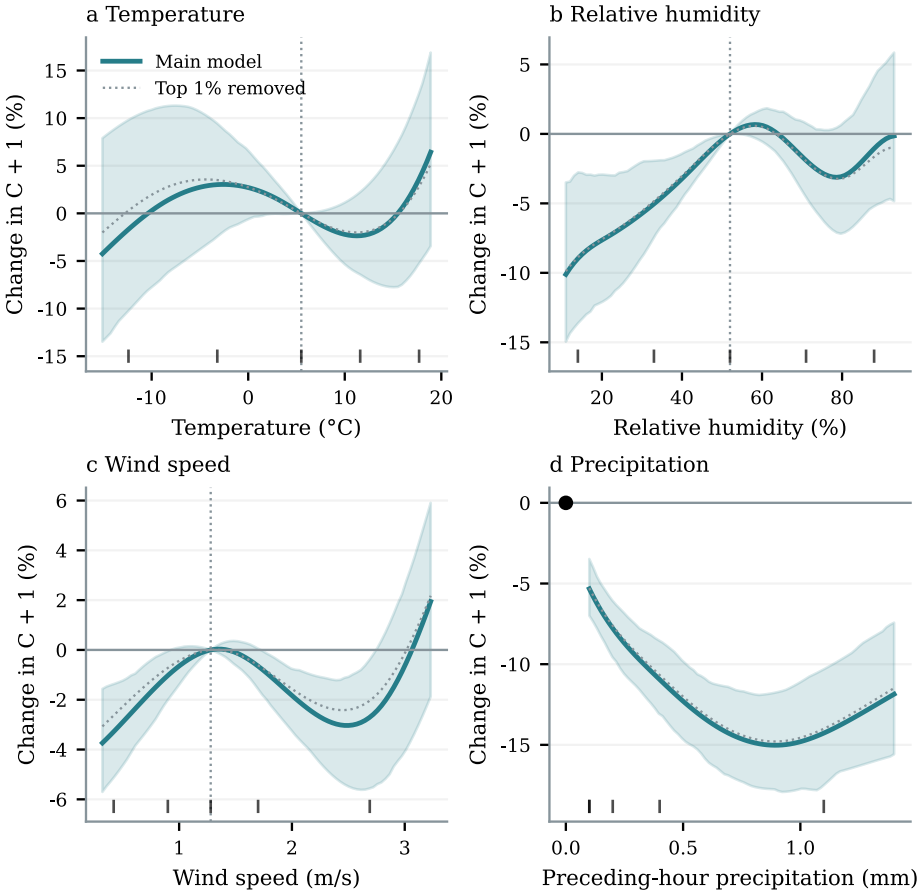


Figure 3: Conditional associations for the four instantaneous meteorological predictors with pointwise 95% confidence intervals. Median references are used for temperature, humidity and wind; precipitation uses a dry-hour reference including the wet-hour term. Solid and dotted lines denote the primary and top-1%-excluded fits, respectively. The precipitation zero point is not joined to the positive-value curve

3.4 Antecedent associations and decomposition of perturbation effects

Figure S1 (Supplementary Information) shows the conditional curves of the four 24-hour antecedent predictors. Over their 10th–90th percentile ranges, the antecedent temperature contrast is +35.7% (+8.8 to +72.0), the humidity contrast −11.6% (−18.9 to −3.2), the wind contrast −9.1% (−14.1 to −4.3) and the antecedent-precipitation contrast (positive preceding-24-h totals, 0.2 to 7.2 mm, 10th–90th percentiles) −13.5% (−19.4 to −7.4); the wet-hour indicator coefficient is small ($\beta_w = -0.014$, 95% CI −0.056 to +0.031). Unlike the instantaneous terms, the antecedent humidity, wind and precipitation contrasts exclude zero. The very large temperature contrast is imprecisely estimated (its interval includes zero with 30-day blocks; Table S8) and is entangled with the seasonal controls: 24-hour mean temperature is strongly correlated with the annual cycle, and the spline and the harmonics can trade association between them. These contrasts use 1,000 seven-day-block replicates, matching Figure S1.

Decomposing each 2024 perturbation into instantaneous and antecedent contributions (Table 2) resolves the apparent tension noted in Section 3.3. Wind-speed effects are almost entirely antecedent: the instantaneous contribution is +0.002 µg/m³ against a total of −0.103 µg/m³. Relative humidity also acts mainly through its antecedent term (−0.131 of the −0.088 µg/m³ total, offset by +0.043 µg/m³ instantaneous), whereas the temperature effect is mostly instantaneous (+0.037 of +0.060

μg/m³) and the precipitation effect, though small, is also mostly antecedent (−0.025 of −0.032 μg/m³). A significant wind perturbation effect is therefore consistent with a non-significant instantaneous wind contrast: the fitted decomposition assigns almost all of the wind sensitivity to the antecedent term rather than to the current hour.

These decompositions are local sensitivity calculations under the fitted model and the specified perturbation amplitudes. The antecedent contrasts use the full 10th–90th percentile range of 24-hour means, which is narrower than the instantaneous range but still spans conditions that are not jointly realized within the same season; the intervals therefore describe partial model associations and not independent physical effects. Bootstrap intervals separate the two components (Table S6). For humidity and wind, the antecedent contribution excludes zero whereas the instantaneous contribution does not; for precipitation, both components are negative and exclude zero, with the antecedent component about 3.5 times larger. For all three, the paired instantaneous-minus-antecedent difference excludes zero; temperature is the exception, with a difference interval that includes zero.

Table 2: Decomposition of the 2024 perturbation effects into instantaneous and antecedent contributions, with eligible-sample support

Perturbation	Total $\Delta PM_{2.5}$	Instant.	Anteced.	95% CI	Eligible	Excl.	RH cap.
Temperature +1°C	+0.060	+0.037	+0.023	[−0.042, +0.152]	8,784	0	—
Humidity +5 pp	−0.088	+0.043	−0.131	[−0.198, +0.034]	8,768	16	176
Wind +10%	−0.103	+0.002	−0.106	[−0.173, −0.040]	8,773	11	—
Precipitation +10%	−0.032	−0.007	−0.025	[−0.042, −0.020]	8,783	1	—

Total and component changes are in μg/m³ and are means over the eligible hours. For each eligible hour, four retransformed predictions are formed from the actual 2024 weather: both blocks unchanged (C00), only the instantaneous block changed (C10), only the antecedent block changed (C01) and both changed (C11). The instantaneous contribution is ½[(C10−C00)+(C11−C01)], the antecedent contribution is ½[(C01−C00)+(C11−C10)], and the two contributions sum exactly to the total change C11−C00 before rounding; the displayed values may differ by less than 0.001 μg/m³ because of rounding. Conditional intervals are those of the total effect; eligible, excluded and relative-humidity-capped hour counts are referenced to the complete 2024 meteorological series.

3.5 Fit quality and internal temporal checks

The selected smoothing parameter is $\lambda=10^{-5}$, with 67.5 effective degrees of freedom. In-sample hourly RMSE is 6.21 μg/m³, MAE 3.77 μg/m³ and R^2 0.327; paired daily RMSE is 3.48 μg/m³ and R^2 0.457. In-sample and internal temporal-evaluation metrics for all models are reported in Table 3. Temporal evaluation uses only preceding years for training, but its role in parameter selection may yield lower errors than evaluation on independent samples. The Duan retransformation factor is 1.087. A nested comparison over the same hours quantifies the contribution of the two weather blocks: with only temporal controls the 2025 hourly RMSE is 5.78 μg/m³; adding only current-hour weather reduces it to 5.57, adding only antecedent weather to 5.39, and adding both to 5.35 (Table S7). The paired bootstrap difference between the antecedent-only and current-only models is −0.18 μg/m³ (95% CI −0.28 to −0.08), whereas the internal 2021–2024 windows cannot distinguish the two blocks (difference −0.003, CI −0.04 to +0.04).

Per-term effective degrees of freedom are 5.6, 6.5, 5.6 and 5.0 for instantaneous temperature, humidity, wind and log precipitation, and 6.1, 5.9, 5.8 and 6.1 for the four antecedent terms; the

temporal controls use 20.0 and the wet-hour indicator 1.0 (values are rounded; total 67.5). The linear benchmark, which replaces the smooth terms with linear terms for the same eight predictors, has in-sample RMSE of 6.29 μg/m³ and 2025 RMSE of 5.47 μg/m³, close to the additive model's 6.21 and 5.35. The penalized splines therefore mainly describe the non-monotonic shapes of the estimated curves rather than adding much predictive skill over a linear model.

Table 3: Hourly model performance for in-sample fitting and internal temporal evaluation

Model	Evaluation	n	RMSE	MAE	MBE	R^2
Calendar	In sample	51,955	6.40	3.92	−0.13	0.285
Linear	In sample	51,955	6.29	3.82	−0.13	0.310
Additive spline	In sample	51,955	6.21	3.77	−0.13	0.327
Random forest	In sample	51,955	5.00	2.90	+0.01	0.564
Calendar	Internal check	34,770	6.61	3.81	−0.78	0.179
Linear	Internal check	34,770	6.56	3.78	−0.94	0.191
Additive spline	Internal check	34,770	6.55	3.78	−0.99	0.193
Random forest	Internal check	34,770	6.25	3.85	+0.19	0.264

The units are μg/m³ for RMSE, MAE and MBE. In-sample metrics reflect the time period 2019–2024 (daily metrics use 2,171 days with at least 18 valid hours); internal temporal metrics consist of a pool of the evaluation windows 2021–2024 (34,770 hourly pairs).

In the pooled internal temporal checks, the additive model gives hourly RMSE of 6.55 μg/m³ and R^2 of 0.193, compared with RMSE of 6.61 and 6.56 μg/m³ for the calendar and linear benchmarks, respectively. The additional predictive gain from nonlinear structure is therefore small. Random forest gives lower RMSE (6.25 μg/m³) and higher R^2 (0.264), while the additive model provides explicit estimates of conditional meteorological associations. Mean four-year RMSE differs by no more than 0.0014 μg/m³ between the two best λ candidates, indicating weak separation of these candidates. This selection uncertainty is not included in the fixed-λ conditional intervals.

Internal errors vary strongly by year (Table 4): additive-model hourly RMSE is 6.10, 5.33, 8.13 and 6.32 μg/m³ in 2021–2024, with MBE +1.19, +0.02, −2.86 and −2.31 μg/m³. The largest error occurs in 2023, the year with the fitting-period maximum (311 μg/m³); excluding it reduces pooled 2021–2024 RMSE to about 5.9 μg/m³, still above 5.35 for 2025. Log-residual autocorrelation is 0.825 at 1 h, 0.409 at 24 h and 0.275 at 168 h (Figure 4), so the effective sample size is far below 51,955. Underestimation in high-concentration groups limits episode reconstruction; unobserved emissions and grid–urban differences are possible contributors (Chen et al., 2022; Zhang et al., 2025).

Table 4: Hourly RMSE (µg/m³) of the four models by evaluation year in the expanding-window internal checks

Year	Calendar	Linear	Additive	Random forest	n
2021	6.19	6.08	6.10	6.39	8,689
2022	5.55	5.37	5.33	5.12	8,693
2023	8.19	8.12	8.13	7.77	8,708
2024	6.19	6.34	6.32	5.38	8,680

n is the number of paired hours in the evaluation year. Each model is trained only on years preceding the evaluation year; the same expanding windows are used to select λ.

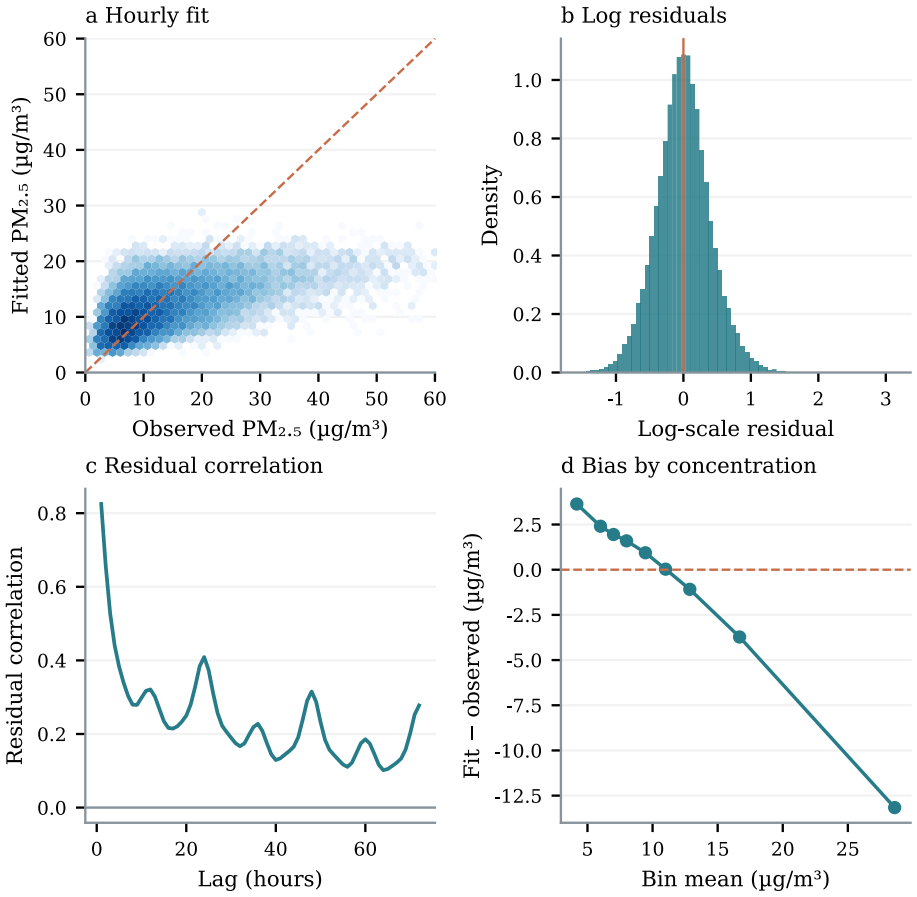


Figure 4: Model diagnostics: (a) hexagonal density of observed and fitted concentrations with a 1:1 reference line; (b) log-residual distribution; (c) residual correlations at actual hourly lags; and (d) mean fitting bias within observation deciles. Panel (a) shows the 0–60 µg/m³ window on both axes; fitting and evaluation retain the full valid sample

3.6 Meteorological normalization and controlled perturbations

Observed annual means fall from 12.16 µg/m³ in 2019 to 8.55 in 2022 and rebound to 10.36 in 2024, whereas normalized means decline almost monotonically from 10.98 to 9.66 µg/m³ (Figure 5; Table 5); the six annual differences are +1.18, +1.08, −0.63, −1.59, +0.13 and +0.70 µg/m³. The normalized

series is nearly log-linear by construction, ($\hat{C}$_norm + 1) ≈ constant × exp(βττ). The trend is βτ = −0.0219 per year (95% CI −0.0330 to −0.0106 with seven-day blocks; −0.0435 to −0.0037 with thirty-day blocks), i.e. −2.17% per year on the C+1 scale (−3.25% to −1.06%).

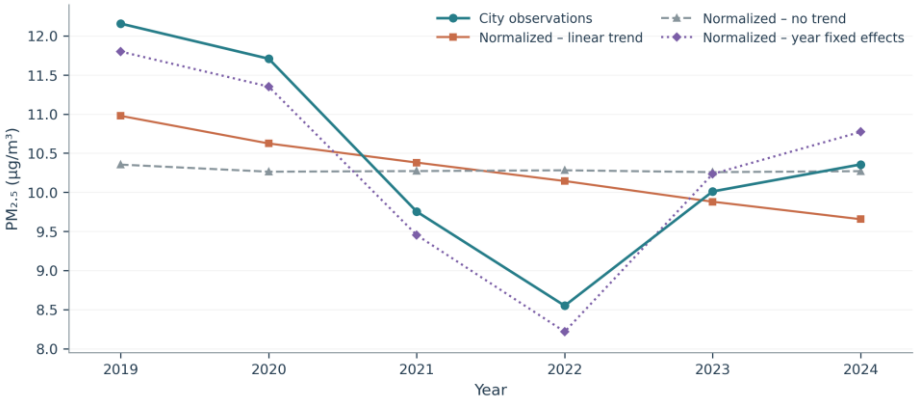


Figure 5: Annual observed concentrations and weather-normalized predictions under three long-term specifications, 2019–2024: linear trend (solid), no trend (dashed) and year fixed effects with 2019 as reference (dotted). All three use the same month–hour normalization draws (288 strata × 200 draws); observations are identical across settings.

The post-2022 divergence between observed and normalized means is therefore a structural consequence of the linear trend term rather than evidence of a meteorological contribution: the trend fitted through 2019–2024 continues downward in years when observed concentrations flattened and then increased. The six-year differences (up to ±1.6 µg/m³) are an order of magnitude larger than the perturbation effects (0.03–0.10 µg/m³). An alternative definition of the meteorological effect, the difference between the mean prediction under actual weather and under normalized weather, is not affected by the observed-minus-fitted residual, although on the original scale it remains scaled by the fitted temporal level and depends on terms estimated jointly with the trend; this effect declines from +0.39 µg/m³ in 2019 to −0.35 µg/m³ in 2024 (Table 5, last column), a decline repeated under the other two specifications (Table S5). The normalized series should therefore be read as a model construct, not as an emission- or climate-adjusted trend (Grange and Carslaw, 2019; Zhai et al., 2019).

The normalized series is therefore specification-dependent. With no long-term term the normalized means are almost flat (10.35 to 10.27 µg/m³ over 2019–2024), whereas year fixed effects produce non-monotonic means with a 2022 minimum (11.80 to 10.77 µg/m³; 8.22 µg/m³ in 2022). The weather-effect estimates show the same sign change across all three specifications (+0.39 to −0.35, +0.45 to −0.43 and +0.31 to −0.44 µg/m³), and the four controlled perturbations keep their sign; the 2025 hourly RMSE is 5.35, 5.25 and 5.26 µg/m³ for the linear, no-trend and year-fixed-effects specifications (Table S5). The normalized decline should therefore be read as conditional on the linear long-term term rather than as a specification-independent trend.

Table 5: Six-year observed, weather-normalized and trend-structure diagnostics

Year	Observed	Normalized	Observed minus normalized	Fitted under actual weather	Fitted minus normalized
2019	12.16	10.98	+1.18	11.36	+0.39
2020	11.71	10.62	+1.08	10.81	+0.18
2021	9.75	10.38	−0.63	10.47	+0.09
2022	8.55	10.14	−1.59	10.16	+0.02
2023	10.01	9.88	+0.13	9.64	−0.24
2024	10.36	9.66	+0.70	9.31	−0.35

All values are in μg/m³ and use identical valid hours within each year. 'Fitted under actual weather' is the mean model prediction at the target timestamps with observed weather; 'Fitted minus normalized' is its difference from the normalized mean; it excludes the observed-minus-fitted residual but not the influence of the fitted trend level. Differences are computed from unrounded values.

The controlled perturbations give mean modeled concentration changes of +0.060 μg/m³ for temperature, −0.088 μg/m³ for relative humidity, −0.103 μg/m³ for wind speed and −0.032 μg/m³ for precipitation (Figure 6). Conditional 95% confidence intervals include zero for temperature and humidity and lie below zero for wind and precipitation (Table 2). These effects combine changes in instantaneous and antecedent predictors, and the decomposition in Section 3.4 assigns the wind and humidity responses mainly to the antecedent terms; they describe local sensitivity under the fitted model, the specified perturbation sizes and the eligible predictor support.

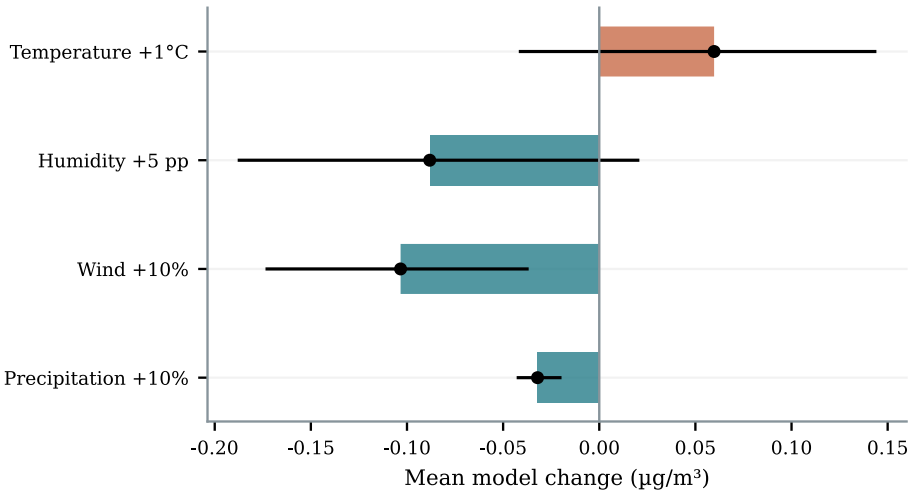


Figure 6: Effects of controlled perturbations to the 2024 weather series. Points indicate mean modeled concentration changes; horizontal lines indicate conditional 95% confidence intervals with knots, λ and retransformation factor fixed

3.7 Evaluation results for public data from 2025

The 2025 dataset comprises 365 city daily archives and 8,760 complete meteorological hours, including 8,451 with valid concentration and complete predictors, giving 96.47% paired coverage. The 309 missing concentration hours remain unfilled. Daily evaluation includes 358 eligible days. The observed annual mean is 10.10 μg/m³, compared with a primary-model mean of 9.50 μg/m³ over

identical hours. Frozen-model metrics are presented in Table 6, with calibration and diagnostics in Figures 7 and 8.

The 2025 record is less extreme than the fitting period: the maximum is 84 μg/m³ (21:00 CST on 19 December 2025), the 99th and 99.9th percentiles are 39 and 67 μg/m³, and 474 hours (5.6%) are at or above 23 μg/m³, compared with 3,137 such hours across 2019–2024 (a mean of 523 per year) and a fitting-period maximum of 311 μg/m³. The 2025 diurnal cycle peaks at 22:00 CST (15.84 μg/m³) and is lowest in the late afternoon at 17:00 (6.25 μg/m³), whereas in 2019–2024 the minimum occurs early in the morning (07:00, 7.10 μg/m³) with a nearly equal afternoon low (16:00–17:00, 7.77–8.05 μg/m³).

Table 6: Hourly and daily evaluation metrics for the frozen models in 2025

Model	Scale	n	RMSE	MAE	MBE	R^2
Calendar	Hourly	8,451	5.78	3.37	−1.09	0.324
Linear	Hourly	8,451	5.47	3.22	−0.81	0.394
Additive spline	Hourly	8,451	5.35	3.16	−0.60	0.421
Random forest	Hourly	8,451	4.78	3.39	+1.24	0.537
Calendar	Daily	358	3.39	2.37	−1.12	0.413
Linear	Daily	358	2.91	2.01	−0.82	0.567
Additive spline	Daily	358	2.80	1.96	−0.62	0.598
Random forest	Daily	358	3.04	2.39	+1.24	0.527

RMSE, MAE and MBE are in μg/m³; R^2 is dimensionless. Hourly n denotes paired hours and daily n denotes days with at least 18 paired hours. All models use identical samples. Paired seven-day block-bootstrap differences in hourly RMSE: additive − linear −0.12 (−0.20 to −0.04); additive − random forest +0.57 (−0.01 to +1.09).

The primary additive model gives hourly RMSE of 5.35 μg/m³, MAE of 3.16 μg/m³, MBE of −0.60 μg/m³ and R^2 of 0.421; daily RMSE is 2.80 μg/m³ and R^2 is 0.598. The hourly RMSE values for the calendar and linear benchmarks are 5.78 and 5.47 μg/m³, respectively, indicating a modest additional gain from nonlinear structure. Random forest has lower hourly RMSE (4.78 μg/m³), but higher hourly MAE (3.39 μg/m³) and daily RMSE (3.04 μg/m³) than the additive model. Model ranking therefore depends on the error measure and temporal scale.

Metrics depend strongly on concentration level. For the 474 hours at or above 23 μg/m³, additive-model RMSE is 18.59 μg/m³ and MBE −16.06 μg/m³, versus 3.13 and +0.32 μg/m³ for the remaining 7,977 hours. The random forest partly reverses this (event RMSE 12.21, MBE −8.04; non-event 3.92, +1.79), so its lower overall RMSE reflects better high-concentration performance rather than uniformly better skill. A calibration curve (Figure 7) shows absolute biases below 0.6 μg/m³ in the lower eight deciles, −1.0 in the ninth and −5.7 in the highest (mean predicted 16.6, observed 22.3 μg/m³).

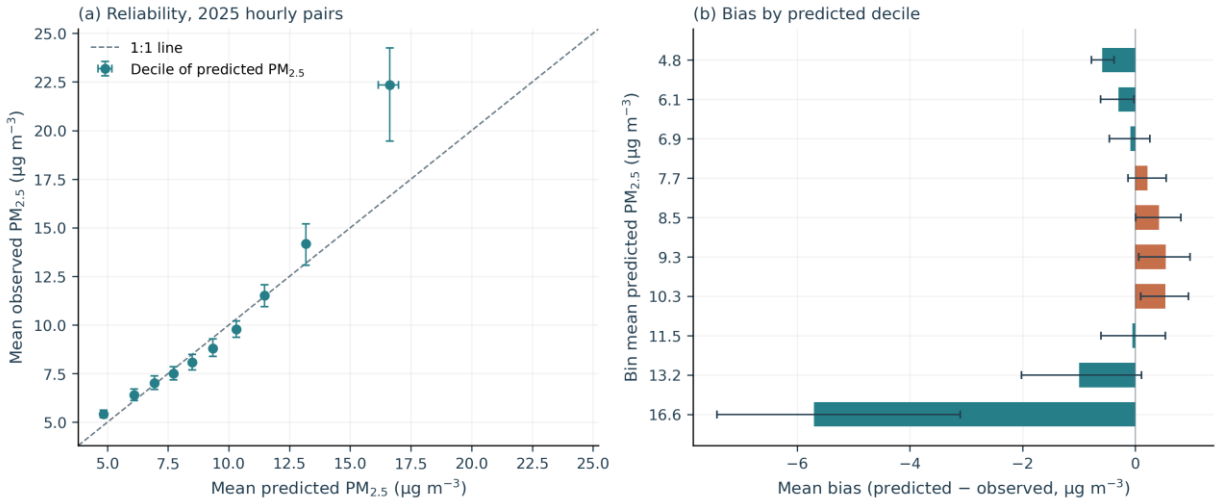


Figure 7: Calibration of frozen-model predictions for 2025. (a) Mean observed versus mean predicted concentration within predicted-concentration deciles; horizontal and vertical error bars describe the predicted and observed bin means, respectively. The dashed line is the 1:1 relation. (b) Mean bias (predicted minus observed) within each decile. Bars are 95% percentile intervals from 1,000 seven-day calendar-block bootstrap resamples, with the model and decile limits fixed. These are descriptive calibration intervals, excluding model-coefficient uncertainty; methods and 14-day sensitivity are provided in the Supplementary Information and Supplementary Data.

Primary-model hourly RMSE is 4.13, 2.52, 3.73 and 8.81 µg/m³ in spring, summer, autumn and winter, respectively; winter MBE is −2.57 µg/m³. For the same 474 hours (at or above the 2025 observed 95th percentile, 23 µg/m³), mean bias is −16.06 µg/m³. Because this grouping conditions on observed concentrations, the negative bias at the upper tail is expected in part from regression to the mean and does not by itself demonstrate systematic underestimation; the event/non-event split shares this limitation. The calibration by predicted decile (Figure 7), which conditions on predictions rather than observations, avoids it and still shows a −5.7 µg/m³ bias in the highest decile (95% calendar-block bootstrap interval −7.4 to −3.1 µg/m³; 14-day blocks give −7.8 to −1.8 µg/m³; Figure 7b). This grouping is an error diagnostic and does not independently identify emission or boundary-layer mechanisms.

The 2025 bias is governed by the trend specification (Table 7). A year-fixed-effects variant gives hourly RMSE 5.26 µg/m³, MBE +0.83, daily RMSE 2.73 and winter MBE −0.68. Freezing the linear trend at 31 December 2024 changes the annual mean bias from −0.60 to −0.49 µg/m³; removing the trend flips it to +0.27. Hourly and daily RMSE and R^2 change little across variants (hourly RMSE 5.25–5.35; R^2 0.421–0.442), and winter MBE remains negative for all four variants (−2.57, −2.45, −1.46 and −0.68 µg/m³, respectively; Table 7). The bias therefore reflects the level implied by the 2019–2024 trend rather than the extra half-year of extrapolation; removing the trend reduces winter bias by about 1.1 µg/m³.

Table 7: Sensitivity of the 2025 evaluation to treatment of the long-term trend

Variant	Hourly RMSE	Hourly MBE	Daily RMSE	R^2	Winter MBE
Primary frozen	5.35	−0.60	2.80	0.421	−2.57
Trend frozen	5.32	−0.49	2.76	0.426	−2.45
No trend	5.25	+0.27	2.67	0.442	−1.46
Year fixed effects	5.26	+0.83	2.73	0.440	−0.68

All variants use the same training data, knots, λ and retransformation factor, except that the trend-frozen variant holds the 2025 trend value at its 31 December 2024 level, the no-trend variant refits the model without the trend column, and the year-fixed-effects variant replaces the linear trend with 2020–2024 dummy variables and freezes the 2024 year effect for 2025. RMSE and MBE are in µg/m³; n = 8,451 hourly pairs and 358 days for all variants. The no-trend and year-fixed-effects refits keep the primary model's Duan retransformation factor (1.087), so differences between variants do not arise from the retransformation step.

A seasonal retransformation factor estimated from 2019–2024 winter residuals (winter 1.14 versus 1.09 overall) reduces the estimated winter MBE from −2.57 to −1.95 µg/m³, indicating that part of the winter bias reflects conditional heterogeneity in the log-scale residuals rather than a pure level error.

Meteorology exceeds training marginal ranges for 87 paired hours (1.03%). The 8,364 hours within those ranges give RMSE of 5.37 µg/m³ and R^2 of 0.421, close to the full-sample estimates, indicating limited sensitivity to this filter. The evaluation supports estimation of part of the variation in a subsequent year under consistent grid meteorology, while winter and high-concentration biases persist. The lower error compared with the internal checks is consistent with the different composition of the evaluation samples — fewer high-concentration hours and slightly lower observed variance in 2025 — rather than with better transferability, and a single evaluation year provides only one realization of meteorological and emission variability. This test does not validate observed meteorological inputs from a central-city station.

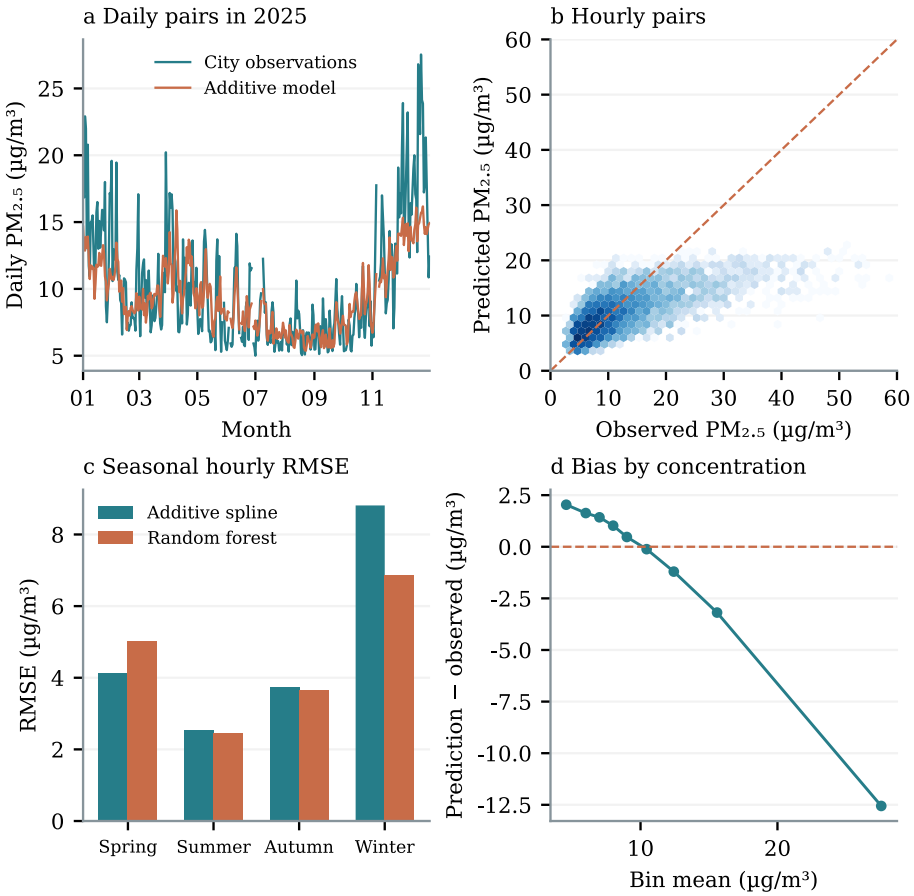


Figure 8: Frozen-model evaluation using public city observations and consistent ERA5 inputs in 2025. Panels show (a) eligible paired daily observations and primary-model predictions, (b) hourly observed–predicted hexagonal density with a 1:1 line, (c) seasonal hourly RMSE for the additive spline and random forest, and (d) primary-model mean prediction bias by observed concentration quantile group. All panels use 2025 observations without model refitting. Panel (b) shows the 0–60 µg/m³ window on both axes; evaluation retains all 8,451 valid hourly pairs

4 Discussion

Two structural features govern the interpretation of the interannual results. First, the single linear long-term term makes the normalized annual means an almost deterministic exponential function of the trend coefficient (Section 3.6; Table 5); the normalized series therefore cannot be used as an emission- or climate-adjusted trend. Reporting the coefficient ($\beta\tau = -0.0219$ per year), all six normalized values and an alternative weather-effect definition that does not depend on the observed-minus-fitted residual makes this explicit. Table S5 shows that this shape depends on the specification; a flexible long-term term remains the natural next step. Zhang et al. (2023) used Unix time as a proxy for the emission trend in a random-forest normalization of Plateau cities; the present results show that the form of such a time term itself shapes the normalized series and the sign of the 2025 bias, which matters whenever these models are used for emission attribution (see also Zheng et al., 2023).

Second, the 2025 bias is governed by the trend specification: freezing the trend changes the mean bias by only 0.11 µg/m³, removing it changes the bias by 0.87 µg/m³, while RMSE and R^2 are essentially unchanged (Table 7). Overall prediction error therefore changes little across variants, whereas the bias follows the long-term term; similar RMSE alone does not show that the weather

attribution is equally reliable, and conclusions about transferability should rest on all variants rather than on the headline bias of the primary model.

For wind, and on point estimates also for humidity, the modeled response is carried mainly by the 24-hour antecedent terms; instantaneous contrasts are small and their intervals include zero, partly because each instantaneous predictor is strongly correlated with its antecedent mean and with seasonal controls (concurvity; Section 3.3). These results support a persistence-based interpretation and caution against reading the instantaneous curves as independent causal effects. The predictive advantage of the antecedent block is clear in 2025 (Table S7) but not in the pooled 2021–2024 windows, and at the daily scale the antecedent-only model (RMSE 2.77 μg/m³) is marginally better than the model with both blocks (2.80 μg/m³); because the 24-hour window was pre-specified rather than selected, the result describes persistence within the fitted model rather than an optimal physical lag.

Errors are dominated by a small number of hours: the 474 hours at or above 23 μg/m³ (5.6% of 2025 hours) account for about two-thirds (68%) of the squared error, the additive model underpredicts the top decile by 5.7 μg/m³, and the random forest trades a level bias for better extreme-hour performance. Model ranking therefore depends on metric, temporal scale and treatment of serial dependence, and calibration and event/non-event metrics should accompany RMSE. The lower out-of-sample error partly reflects the fewer extreme hours and lower variance of 2025 rather than better transferability.

The six-year record also requires external comparison. Lhasa statistical communiqués report annual means of 12, 12, 10, 8, 10 and 11 μg/m³ for 2019, 2020, 2021, 2022, 2024 and 2025 (no value for 2023; Table S4). After rounding these agree with the present series except 2022 (8.55 versus 8) and 2025 (10.10 versus 11). Rounding cannot explain these two differences, and a daily-mean recalculation changes the annual means by at most 0.06 μg/m³, so the averaging method does not explain them either; the remaining candidates, audited versus real-time data and changes in the station set, cannot be separated with the present data. The analysis therefore refers to the real-time release archive. Older Lhasa studies used standard-state concentrations (Duo et al., 2018; Yin et al., 2019); an approximate 0.62 conversion factor for 650 hPa and 281 K indicates that part of the apparent difference may be metric rather than physical.

Several limitations remain. The ERA5 cell is 14.6 km from the requested point and 583 m higher (equivalent to about 3.8 K under a standard lapse rate, not a measured bias); ERA5-Land and 10 m wind direction were not used in the main model, although adding boundary-layer height to the primary specification, with both versions refitted on the 47,596 training hours that have boundary-layer data and evaluated on the same 8,451 hours, reduces 2025 hourly RMSE from 5.456 to 5.382 μg/m³ and increases R^2 from 0.398 to 0.414 (Table S11; this comparison uses a same-subset primary refit rather than the full-sample 5.35 μg/m³), and residuals are largest under shallow boundary layers and south-easterly winds (Tables S2 and S3). A partial ERA5-Land check, which replaces ERA5 temperature and humidity while retaining ERA5 wind and precipitation (in ERA5-Land these two come from the ERA5 forcing, and the Open-Meteo archive does not provide them separately), changes 2025 hourly RMSE from 5.35 to 5.40 μg/m³ and R^2 from 0.421 to 0.410; the wind and humidity contrasts keep their sign, whereas the temperature contrast is more sensitive to the meteorological product (Table S9). Emissions, the 2022 static-management period (Chen et al., 2023; Lhasa Municipal Leading Group Office for COVID-19 Prevention and Control, 2022) and directional transport are not represented; Table S1 shows where these omissions matter most. Residual autocorrelation (0.275 at 168 h) reduces the effective sample size; a single evaluation year provides one realization; block length is examined in Table S8, while seasonal smearing is only partly addressed. Religious and residential burning is documented in Lhasa, but source observations are summer-only (Cui et al., 2018; Xia et al., 2024) whereas the peak is in winter, and high emission

factors for yak dung, WeiSang and incense (Zhang et al., 2022) suggest winter contributions may be underestimated.

5 Conclusion

During 2019–2024, Lhasa city-average $PM_{2.5}$ shows winter maxima, summer minima, a clear diurnal cycle and nonmonotonic interannual variation. After controlling temporal structure and meteorology, the additive model estimates conditional associations that vary across predictor ranges: the positive-precipitation contrast is negative, and the instantaneous temperature, humidity and wind intervals include zero. In perturbation decompositions the antecedent components dominate the wind and precipitation effects (paired differences exclude zero; Table S6); for humidity the antecedent component is the larger point estimate and the only one whose interval excludes zero, although its |antecedent|−|instantaneous| interval includes zero, so within the fitted model these responses are carried mainly by antecedent conditions.

With parameters frozen after 2019–2024, the model gives 2025 hourly RMSE 5.35 μg/m³ (R^2 = 0.421; 8,451 hours) and daily RMSE 2.80 μg/m³ (R^2 = 0.598; 358 days). It improves on the calendar and linear benchmarks, although the linear gain is modest; the random forest's lower hourly RMSE comes from better performance in high-concentration hours and is accompanied by a +1.24 μg/m³ level bias. Trend-frozen and no-trend variants change the annual mean bias from −0.60 to −0.49 and +0.27 μg/m³ with little RMSE change; errors concentrate in 474 high-concentration hours, and Gutor-evening residuals exceed the same-hour winter background in five of six years and average +30.0 μg/m³ (+7.0 μg/m³ excluding the 2023 episode).

The results support conditional meteorological characterization and retrospective estimation using consistent grid meteorology. Interpretation remains limited by the single linear trend, by reanalysis–observation differences, by omitted emissions and boundary-layer processes and by a single evaluation year. A six-year series and controlled perturbations do not identify the causal impact of long-term climate change; further work should combine urban observations, emission information and multi-year validation.

Data availability

Hourly city-average $PM_{2.5}$ records are publicly available from the QuotSoft archive (https://quotsoft.net/air/), which redistributes real-time releases of the China National Environmental Monitoring Centre. ERA5 data are available from the Copernicus Climate Data Store (https://doi.org/10.24381/cds.adbb2d47) and were retrieved through the Open-Meteo Historical Weather API. Supplementary Data 1 (Supplementary Information) contains Tables S1–S12 and Figures S1–S2. Supplementary Data 2 (validation package) contains the analysis-ready inputs, the fixed model state, saved hourly predictions, the calibration-bootstrap source data and runnable checks for the frozen-model evaluation, normalization and decomposition recomputations (with file-level SHA-256 checks in its manifest). The analysis code, model objects and processed hourly series will be made publicly available at Zenodo upon acceptance.

CRediT authorship contribution statement

Zhongjie Ma: Conceptualization, Methodology, Software, Validation, Formal analysis, Investigation, Data curation, Writing – original draft, Writing – review & editing, Visualization.

Declaration of competing interest

The author declares that he has no known competing financial interests or personal relationships that could have appeared to influence the work reported in this paper.

Funding

This research did not receive any specific grant from funding agencies in the public, commercial, or not-for-profit sectors.

Acknowledgements

The author thanks the Open-Meteo project for providing access to ERA5 and open meteorological archives. This study contains modified Copernicus Climate Change Service information (2026). Neither the European Commission nor ECMWF is responsible for any use that may be made of the Copernicus information or data it contains.

Declaration of generative AI and AI-assisted technologies in the manuscript preparation process

The author conceived and designed the study, collected and processed the data, selected the methods and formulas, carried out the original analyses and wrote the first draft of the manuscript. During the preparation of this work, the author used an AI coding assistant (DeepSeek-V4.1-Flash1017) to develop and modify analysis code, verify data and numerical results and polish the language, and used AI chat assistants, including ChatGPT (OpenAI), to review the analysis and manuscript text, check reported numbers and suggest revisions to the analyses and wording. The author evaluated every suggestion before adopting it, checked all outputs, and takes full responsibility for the content of the publication.

References

Barmpadimos, I., Hueglin, C., Keller, J., Henne, S., Prévôt, A.S.H., 2011. Influence of meteorology on PM10 trends and variability in Switzerland from 1991 to 2008. Atmospheric Chemistry and Physics 11, 1813–1835. https://doi.org/10.5194/acp-11-1813-2011

Che, J., Zhao, P., 2021. Characteristics of the summer atmospheric boundary layer height over the Tibetan Plateau and influential factors. Atmospheric Chemistry and Physics 21, 5253–5268. https://doi.org/10.5194/acp-21-5253-2021

Chen, S., Wang, W., Li, M., et al., 2022. The contribution of local anthropogenic emissions to air pollutants in Lhasa on the Tibetan Plateau. Journal of Geophysical Research: Atmospheres 127, e2021JD036202. https://doi.org/10.1029/2021JD036202

Chen, X., Zhang, F., Zhang, D., Xu, L., Liu, R., Teng, X., Zhang, X., Wang, S., 2023. Variations of air pollutant response to COVID-19 lockdown in cities of the Tibetan Plateau. Environmental Science: Atmospheres 3, 708–716. https://doi.org/10.1039/D2EA00168C

China Tibet Online, 2023. 拉萨群众迎来一年一度的“古突”之夜 [Lhasa residents welcome the annual Gutor night]. 20 February 2023. http://ttt.tibet.cn/cn/culture/ms/202302/t20230220_7363567.htm (accessed 28 October 2026).

Cui, Y.Y., Liu, S., Bai, Z., Bian, J., Li, D., Fan, K., McKeen, S.A., Watts, L.A., Ciciora, S.J., Gao, R.-S., 2018. Religious burning as a potential major source of atmospheric fine aerosols in summertime Lhasa on the Tibetan Plateau. Atmospheric Environment 181, 186–191. https://doi.org/10.1016/j.atmosenv.2018.03.025

Duan, N., 1983. Smearing estimate: a nonparametric retransformation method. Journal of the American Statistical Association 78, 605–610. https://doi.org/10.1080/01621459.1983.10478017

Duo, B., Cui, L., Wang, Z., et al., 2018. Observations of atmospheric pollutants at Lhasa during 2014–2015: pollution status and the influence of meteorological factors. Journal of Environmental Sciences 63, 28–42. https://doi.org/10.1016/j.jes.2017.03.010

Eilers, P.H.C., Marx, B.D., 1996. Flexible smoothing with B-splines and penalties. Statistical Science 11, 89–121. https://doi.org/10.1214/ss/1038425655

Grange, S.K., Carslaw, D.C., Lewis, A.C., et al., 2018. Random forest meteorological normalisation models for Swiss PM10 trend analysis. Atmospheric Chemistry and Physics 18, 6223–6239. https://doi.org/10.5194/acp-18-6223-2018

Grange, S.K., Carslaw, D.C., 2019. Using meteorological normalisation to detect interventions in air quality time series. Science of the Total Environment 653, 578–588. https://doi.org/10.1016/j.scitotenv.2018.10.344

Hersbach, H., Bell, B., Berrisford, P., et al., 2020. The ERA5 global reanalysis. Quarterly Journal of the Royal Meteorological Society 146, 1999–2049. https://doi.org/10.1002/qj.3803

Hersbach, H., Bell, B., Berrisford, P., Biavati, G., Horányi, A., Muñoz Sabater, J., Nicolas, J., Peubey, C., Radu, R., Rozum, I., Schepers, D., Simmons, A., Soci, C., Dee, D., Thépaut, J.-N., 2023. ERA5 hourly data on single levels from 1940 to present. Copernicus Climate Change Service (C3S) Climate Data Store (CDS). https://doi.org/10.24381/cds.adbb2d47 (accessed 25 October 2026).

Huang, W., Wang, S., Cheng, P., Chen, B., Yuan, B., Yu, P., Wang, H., Ma, N., Li, M., Lu, K., 2025. Measurement report: unexpected high volatile organic compounds emission from vehicles on the Tibetan Plateau. Atmospheric Chemistry and Physics 25, 15403–15414. https://doi.org/10.5194/acp-25-15403-2025

IPCC, 2021. Climate Change 2021: The Physical Science Basis. Contribution of Working Group I to the Sixth Assessment Report of the Intergovernmental Panel on Climate Change. Cambridge University Press. https://doi.org/10.1017/9781009157896

Jacob, D.J., Winner, D.A., 2009. Effect of climate change on air quality. Atmospheric Environment 43, 51–63. https://doi.org/10.1016/j.atmosenv.2008.09.051

Lhasa Municipal Bureau of Statistics, 2020–2026. Lhasa Municipal Statistical Communiqués on National Economic and Social Development, 2019–2025 data years. https://tjj.lasa.gov.cn/tjj/tjgb/ (accessed 25 October 2026).

Lhasa Municipal Leading Group Office for COVID-19 Prevention and Control, 2022. Announcement No. 8 of 2022. 8 August 2022. https://lasa.gov.cn/lasa/c100868/202208/93e725a9e07f445d85b69067254d4e14.shtml

Li, C., Han, X., Kang, S., Yan, F., Chen, P., et al., 2019. Heavy near-surface PM2.5 pollution in Lhasa, China during a relatively static winter period. Chemosphere 214, 314–318. https://doi.org/10.1016/j.chemosphere.2018.09.135

Ministry of Ecology and Environment, 2018. Notice on amendments to ambient air quality and associated monitoring standards (Announcement No. 29 of 2018). 13 August 2018. https://www.mee.gov.cn/xxgk2018/xxgk/xxgk01/201808/t20180815_629602.html (accessed 25 October 2026).

Open-Meteo, 2023. Open-Meteo historical weather data archive. Zenodo. https://doi.org/10.5281/zenodo.7970649

Open-Meteo, 2026. Historical Weather API documentation. https://open-meteo.com/en/docs/historical-weather-api (accessed 14 October 2026).

QuotSoft, 2026. China air quality historical data and data format documentation. https://quotsoft.net/air/ (accessed 14 October 2026).

Ran, L., Lin, W., Deji, Y., La, B., Tsering, P.M., Xu, X., Wang, W., 2014. Surface gas pollutants in Lhasa, a highland city of Tibet – current levels and pollution implications. Atmospheric Chemistry and Physics 14, 10721–10730. https://doi.org/10.5194/acp-14-10721-2014

Ran, L., Deng, Z., Wu, Y., Li, J., Bai, Z., Lu, Y., Zhuoga, D., Bian, J., 2022. Measurement report: vertical profiling of particle size distributions over Lhasa, Tibet – tethered balloon-based in situ measurements and source apportionment. Atmospheric Chemistry and Physics 22, 6217–6229. https://doi.org/10.5194/acp-22-6217-2022

Roberts, D.R., Bahn, V., Ciuti, S., et al., 2017. Cross-validation strategies for data with temporal, spatial, hierarchical, or phylogenetic structure. Ecography 40, 913–929. https://doi.org/10.1111/ecog.02881

Tai, A.P.K., Mickley, L.J., Jacob, D.J., 2010. Correlations between fine particulate matter (PM2.5) and meteorological variables in the United States: implications for the sensitivity of PM2.5 to climate change. Atmospheric Environment 44, 3976–3984. https://doi.org/10.1016/j.atmosenv.2010.06.060

Vu, T.V., Shi, Z., Cheng, J., Zhang, Q., He, K., Wang, S., Harrison, R.M., 2019. Assessing the impact of clean air action on air quality trends in Beijing using a machine learning technique. Atmospheric Chemistry and Physics 19, 11303–11314. https://doi.org/10.5194/acp-19-11303-2019

Xia, K., Liu, C.-C., Mei, S.-S., Bai, Z., Bian, J., Yu, P., Zhao, C., Liu, S., 2024. Physicochemical characterization of religious burning aerosols in Lhasa on the Qinghai-Tibet Plateau. Journal of Geophysical Research: Atmospheres 129, e2024JD041274. https://doi.org/10.1029/2024JD041274

Yin, X., de Foy, B., Wu, K., et al., 2019. Gaseous and particulate pollutants in Lhasa, Tibet during 2013–2017: spatial variability, temporal variations and implications. Environmental Pollution 253, 68–77. https://doi.org/10.1016/j.envpol.2019.06.113

Zhai, S., Jacob, D.J., Wang, X., et al., 2019. Fine particulate matter (PM2.5) trends in China, 2013–2018: separating contributions from anthropogenic emissions and meteorology. Atmospheric Chemistry and Physics 19, 11031–11041. https://doi.org/10.5194/acp-19-11031-2019

Zhang, X., Xu, J., Zhai, L., Zhao, W., 2022. Characterization of aerosol properties from the burning emissions of typical residential fuels on the Tibetan Plateau. Environmental Science & Technology 56, 14296–14305. https://doi.org/10.1021/acs.est.2c04211

Zhang, B., Zhang, Y., Zhang, K., Zhang, Y., Ji, Y., et al., 2023. Machine learning assesses drivers of PM2.5 air pollution trend in the Tibetan Plateau from 2015 to 2022. Science of the Total Environment 878, 163189. https://doi.org/10.1016/j.scitotenv.2023.163189

Zhang, M., Wang, S., Yu, W., et al., 2025. The major role of anthropogenic emission underestimation in PM2.5 estimation uncertainty over the Tibetan Plateau. Geophysical Research Letters 52, e2024GL110513. https://doi.org/10.1029/2024GL110513

Zheng, H., Kong, S., Zhai, S., Sun, X., Cheng, Y., et al., 2023. An intercomparison of weather normalization of PM2.5 concentration using traditional statistical methods, machine learning, and chemistry transport models. npj Climate and Atmospheric Science 6, 214. https://doi.org/10.1038/s41612-023-00536-7

Supplementary Information

Meteorological associations of hourly $PM_{2.5}$ in Lhasa, Tibetan Plateau: antecedent weather, trend specification and out-of-sample evaluation

Zhongjie Ma[1]*

[1] Reading Academy, Nanjing University of Information Science & Technology, Nanjing 210044, China

*Corresponding Author. Email: zhongjiema2023@outlook.com

This Supplementary Information contains Appendix A (supplementary tables and figures) and Appendix B (supplementary methods) for the manuscript above.

Appendix A. Supplementary material

Figure S1 shows the full conditional curves for the four antecedent predictors discussed in Section 3.4, and Figure S2 the study area and reanalysis cells. Table S1 reports event-window residuals, Table S2 boundary-layer-height quintiles, Table S3 wind-sector residuals and Table S4 the comparison with the statistical communiqués. Table S5 reports the three trend specifications, Table S6 the perturbation-component intervals, Table S7 the nested-model comparison, Table S8 the block-length sensitivity, Table S9 the partial ERA5-Land check, Table S10 the ±1 h alignment check, Table S11 the paired boundary-layer-height comparison and Table S12 the analysis stages, software environments and random seeds.

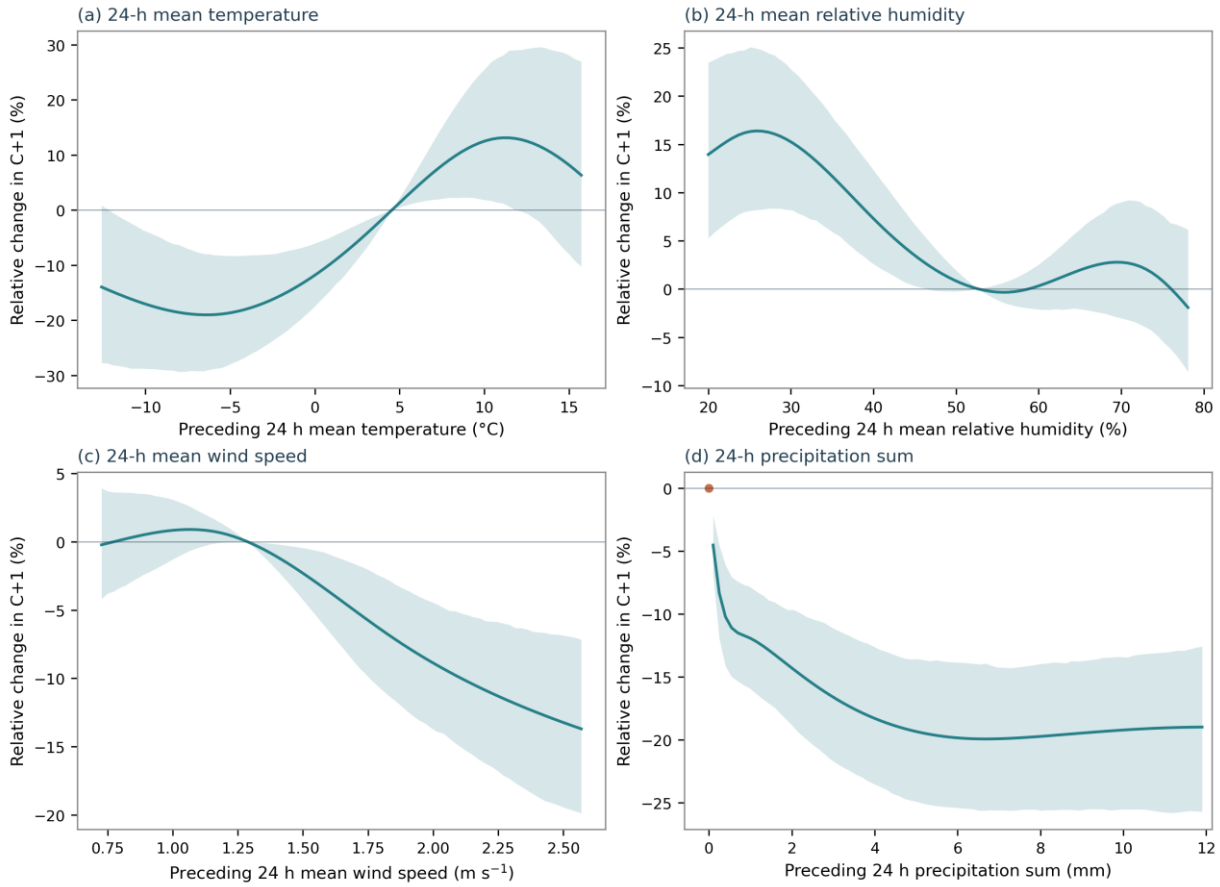


Figure S1: Conditional associations for the four 24-hour antecedent predictors, with pointwise 95% confidence intervals. Temperature, relative humidity and wind speed are referenced to their training-sample medians; the preceding-24-h precipitation curve is referenced to a zero total (0 mm). Shaded bands show conditional 95% confidence intervals from 1,000 seven-day block replicates; the temperature curve is imprecise and non-monotonic, consistent with confounding between 24-hour mean temperature and the seasonal controls.

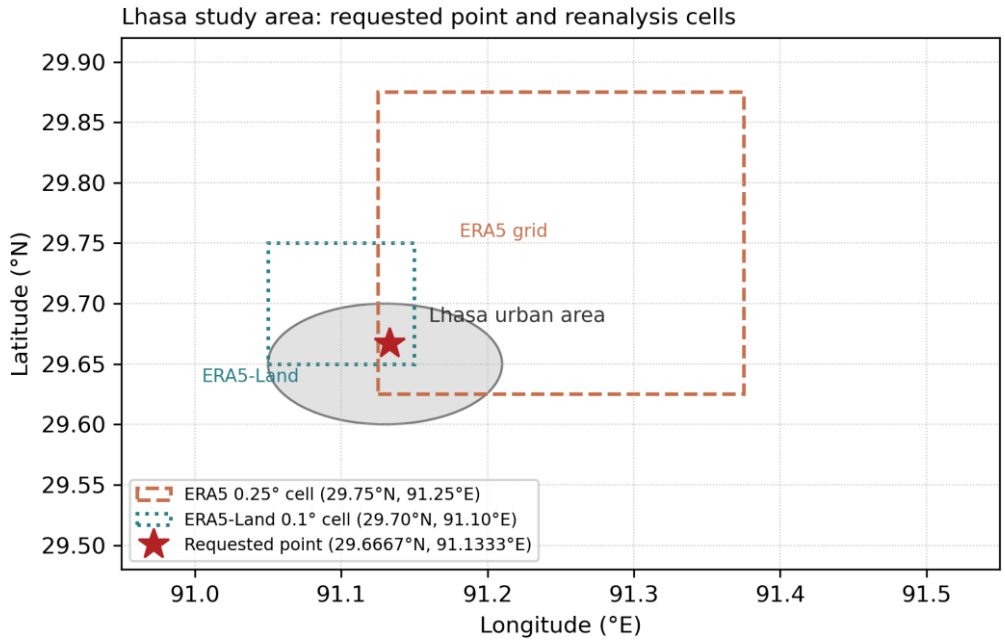


Figure S2: Schematic study-area map: Lhasa urban area, requested point (29.6667°N, 91.1333°E), ERA5 0.25° cell (29.75°N, 91.25°E) and ERA5-Land 0.1° cell (29.70°N, 91.10°E). The city-average series is derived from the national monitoring network; station locations are not shown.

Table S1: Observed-minus-predicted residuals in festival and control windows, 2019–2024

Window	Hours	Mean residual	Same-hour background	Excess	95% CI for excess (μg/m³)
Gutor evening 2019	4	+8.7	+3.5	+5.3	—
Gutor evening 2020	5	+9.6	+7.0	+2.6	—
Gutor evening 2021	5	+22.6	+3.6	+19.0	—
Gutor evening 2022	5	+13.0	+4.9	+8.1	—
Gutor evening 2023	5	+147.3	+7.1	+140.2	—
Gutor evening 2024	5	+8.6	+9.0	−0.4	—
Gutor evening, all years (hour-weighted)	29	+35.9	+5.9	+30.0	[+3.1, +76.6]
Gutor evening, all years (equal-year weight)	29	+35.0	+5.8	+29.1	[+3.4, +74.6]
Losar window, excluding Gutor night	635	+2.9	+0.9	+2.0	[+0.4, +3.9]
Spring Festival, excluding Losar/Gutor hours	214	−1.5	+0.9	−2.4	[−4.5, +0.1]
2020 national control period (24 Jan–31 Mar 2020)	1624	−1.6	—	—	—
2022 static management (8 Aug–20 Sep)	1025	−1.9	—	—	—
2022 extended (8 Aug–21 Oct)	1768	−1.5	—	—	—
Festival-excluded winter background (all clock hours)	12065	+1.0	—	—	—

Residuals are observed minus in-sample prediction from the primary additive model. Gutor evening is defined as 20:00–24:00 on the Gutor date (the 20:00, 21:00, 22:00 and 23:00 labels of that date plus 00:00 of the following day, five hourly labels); the Gutor night, used for festival-window exclusion and background selection, is 18:00 on the Gutor date to 06:00 of the following day (13 hourly labels). The Losar window is day −2 00:00 to day +2 23:00 (120 hourly labels before exclusions); the Spring Festival window runs from the listed Chinese New Year's Eve date at 00:00 through 23:00 two calendar days after that eve date (72 hourly labels before exclusions); festival windows are applied in the order Gutor evening, Losar (excluding the Gutor night) and Spring Festival (excluding hours shared with Losar and Gutor), whereas the 2020 national control period (24

January–31 March 2020) and the 2022 Lhasa static-management period (8 August–20 September 2022) may overlap the festival windows. The same-hour background is the mean residual of festival-excluded winter hours (December–February) in the same year and at the same clock hour; the 2020 control period is not excluded from this background (690 of its hours remain in the 12,065 background hours). Hour-weighted and equal-year means are both reported; the sign test is two-sided (five of six positive, exact binomial $p = 0.22$). Only six Gutor evenings are available, so their intervals resample these events; intervals for the Losar and Spring Festival windows resample days within each window. Dates: Gutor 3 Feb 2019, 22 Feb 2020, 10 Feb 2021, 1 Mar 2022, 19 Feb 2023, 8 Feb 2024; Losar 5 Feb 2019, 24 Feb 2020, 12 Feb 2021, 3 Mar 2022, 21 Feb 2023, 10 Feb 2024; Spring Festival eve 4 Feb 2019, 24 Jan 2020, 11 Feb 2021, 31 Jan 2022, 21 Jan 2023, 9 Feb 2024. Spring Festival and Losar coincide on 5 Feb 2019, 12 Feb 2021 and 10 Feb 2024; those hours are assigned to Losar. The Spring Festival window contains hours only in 2020, 2022 and 2023; in 2019, 2021 and 2024 the whole window falls within the Losar window.

Table S2: Winter residual means by ERA5 boundary-layer-height quintile

ERA5 BLH quintile	Mean BLH (m)	Hours	Mean residual (μg/m³)
Q1 (lowest)	23	3673	+3.14
Q2	50	2526	+0.50
Q3	195	1667	+1.36
Q4	825	1736	−0.96
Q5 (highest)	2698	1840	−0.52

Winter (December–February) hours 2019–2024 with valid ERA5 boundary-layer height. Quintile limits (30, 80, 400 and 1,425 m) are taken from the all-season 2019–2024 distribution, so winter hours are unevenly distributed across quintiles. The Open-Meteo ERA5 archive used here has no boundary-layer values for January–June 2024, so the sensitivity estimates use the remaining hours; the main model is unchanged.

Table S3: Winter residual means by 10 m wind sector

10 m wind sector	Hours (wind ≥ 0.5 m/s)	Mean residual (μg/m³)
E	3420	+1.84
N	611	−1.94
NE	3868	+0.63
NW	140	−1.86
S	1433	+1.78
SE	2009	+3.19
SW	876	−0.56
W	193	−1.51

Sectors use the ERA5 10 m wind direction; calm hours (wind speed < 0.5 m s^{-1}) are excluded.

Table S4: Comparison of annual mean $PM_{2.5}$ with the Lhasa statistical communiqués

Year	Official	This study	Difference	Note	Source communiqué
2019	12	12.16	+0.16		2020
2020	12	11.71	−0.29		2021
2021	10	9.75	−0.25		2022
2022	8	8.55	+0.55	integer bulletin value	2023
2023	n/a	10.01	—	ranking only in bulletin	2024
2024	10	10.36	+0.36		2025
2025	11	10.10	−0.90	validation year	2026

Official values are the 'annual mean $PM_{2.5}$ concentration' reported in the Lhasa municipal statistical communiqués (Lhasa Municipal Bureau of Statistics, 2020–2026), in integer μg/m³; the communiqués do not disclose whether annual means are computed from daily or hourly values. Present-study values are the hourly-mean annual means of Table 1 and Section 3.7; differences are present minus official. Source communiqués: data year 2019 → 13 Apr 2020; 2020 → May 2021; 2021 → Apr 2022; 2022 → 18 Apr 2023; 2023 → ranking only; 2024 → 22 Apr 2025; 2025 → 29 Apr 2026 (https://tjj.lasa.gov.cn/tjj/tjgb/).

Table S5: Six-year observed, weather-normalized and weather-effect values under three long-term specifications

Year	Obs.	Norm. lin.	Norm. no tr.	Norm. YFE	WE lin.	WE no tr.	WE YFE
2019	12.16	10.98	10.35	11.80	+0.39	+0.45	+0.31
2020	11.71	10.62	10.26	11.35	+0.18	+0.20	+0.19
2021	9.75	10.38	10.27	9.45	+0.09	+0.09	+0.09
2022	8.55	10.14	10.28	8.22	+0.02	+0.01	+0.13
2023	10.01	9.88	10.26	10.23	−0.24	−0.27	−0.28
2024	10.36	9.66	10.27	10.77	−0.35	−0.43	−0.44

All three specifications use the same 288 month–hour strata × 200 draws from the 2019–2024 reference period. Weather effect = mean prediction under actual weather minus mean prediction under normalized weather over identical valid hours. Across trend specifications, the total perturbation effects differ by less than 0.02 μg/m³ for wind and precipitation. The humidity effects are −0.088, −0.110 and −0.056 μg/m³, and the temperature effects are +0.060, +0.061 and +0.130 μg/m³, for the linear, no-trend and year-fixed-effects specifications, respectively. The 2025 hourly RMSE is 5.35, 5.25 and 5.26 μg/m³, respectively.

Table S6: Bootstrap intervals for the instantaneous, antecedent and total perturbation components

Perturbation	**Component**	**Estimate (μg/m³)**	**95% CI (μg/m³)**	**Excl. 0**
Temperature +1 °C	Total	+0.0597	[−0.042, +0.152]	no
Temperature +1 °C	Instantaneous	+0.0366	[−0.022, +0.091]	no
Temperature +1 °C	Antecedent	+0.0232	[−0.079, +0.128]	no
Temperature +1 °C	Instantaneous minus antecedent	+0.013	[−0.126, +0.148]	no
Humidity +5 pp	Total	−0.0882	[−0.198, +0.034]	no
Humidity +5 pp	Instantaneous	+0.0432	[−0.021, +0.102]	no
Humidity +5 pp	Antecedent	−0.1314	[−0.240, −0.012]	yes
Humidity +5 pp	|Antecedent| minus |instantaneous|	+0.088	[−0.026, +0.193]	no

Humidity +5 pp	Instantaneous minus antecedent	+0.175	[+0.032, +0.307]	yes
Wind speed +10%	Total	−0.1033	[−0.173, −0.040]	yes
Wind speed +10%	Instantaneous	+0.0024	[−0.017, +0.018]	no
Wind speed +10%	Antecedent	−0.1057	[−0.172, −0.048]	yes
Wind speed +10%	Instantaneous minus antecedent	+0.108	[+0.048, +0.174]	yes
Precipitation +10%	Total	−0.0321	[−0.042, −0.020]	yes
Precipitation +10%	Instantaneous	−0.0071	[−0.010, −0.004]	yes
Precipitation +10%	Antecedent	−0.0250	[−0.035, −0.013]	yes
Precipitation +10%	Instantaneous minus antecedent	+0.018	[+0.006, +0.029]	yes

Components are means over the 2024 eligible hours of a symmetric two-group Shapley decomposition on the concentration scale. For each hour, four retransformed predictions are formed: both blocks unchanged (C00), only the instantaneous block changed (C10), only the antecedent block changed (C01) and both changed (C11). The instantaneous component is ½[(C10−C00)+(C11−C01)], the antecedent component is ½[(C01−C00)+(C11−C10)], and the two components sum to the total change C11−C00 before rounding (display rounding may give a difference below 0.001 μg/m³); the retransformation factor is held fixed at 1.087. Intervals are 2.5–97.5 percentiles of 1,000 seven-day block-bootstrap coefficient replicates, applying the same decomposition within each replicate. Temperature is the exception: its instantaneous-minus-antecedent interval includes zero, whereas the corresponding intervals for humidity, wind and precipitation exclude zero.

Table S7: Nested-model comparison of current-hour and 24-h antecedent weather blocks

Model	2025 hourly RMSE	2025 hourly MAE	2025 hourly R^2	2025 daily RMSE	2025 daily R^2
Temporal controls only	5.78	3.37	0.324	3.39	0.413
Controls + current hour	5.57	3.25	0.371	3.07	0.519
Controls + 24-h antecedent	5.39	3.20	0.411	2.77	0.606
Controls + both	5.35	3.16	0.421	2.80	0.598

All models use the same 51,955 training hours and $\lambda=10^{-5}$; the 2025 evaluation uses 8,451 paired hours. Paired seven-day block-bootstrap 95% differences in 2025 hourly RMSE: both − current −0.22 (−0.32 to −0.11), both − antecedent −0.04 (−0.07 to −0.02), antecedent − current −0.18 (−0.28 to −0.08). The 2021–2024 internal windows cannot distinguish the antecedent-only and current-only models (difference −0.003, CI −0.04 to +0.04).

Table S8: Block-length sensitivity of the reported intervals (1,000 replicates)

Quantity	Estimate	95% CI (7-day)	95% CI (14-day)	95% CI (30-day)
Temperature, current hour (%)	−0.51	[−13.82, +13.99]	[−16.71, +16.59]	[−17.95, +19.54]
Humidity, current hour (%)	+5.54	[−2.72, +13.70]	[−3.45, +14.72]	[−4.35, +16.23]
Wind, current hour (%)	−0.20	[−2.83, +1.95]	[−3.06, +2.37]	[−3.08, +2.50]
Precipitation, current hour (%; wet-hour p25–p75)	−5.94	[−8.41, −3.57]	[−8.22, −3.58]	[−8.59, −3.33]
Temperature, 24-h antecedent (%)	+35.72	[+8.84, +71.95]	[+1.66, +79.96]	[−0.62, +91.12]
Humidity, 24-h antecedent (%)	−11.56	[−18.88, −3.23]	[−19.47, −2.21]	[−20.06, −2.69]
Wind, 24-h antecedent (%)	−9.07	[−14.10, −4.29]	[−14.92, −4.08]	[−14.45, −4.29]
Precipitation, 24-h antecedent (%; positive 24-h totals, p10–p90)	−13.52	[−19.37, −7.40]	[−19.79, −6.88]	[−20.37, −7.39]
Temperature +1°C, total (μg/m³)	+0.0597	[−0.042, +0.152]	[−0.071, +0.179]	[−0.076, +0.184]
Temperature +1°C, instantaneous (μg/m³)	+0.0366	[−0.022, +0.091]	[−0.035, +0.101]	[−0.041, +0.114]
Temperature +1°C, antecedent (μg/m³)	+0.0232	[−0.079, +0.128]	[−0.102, +0.150]	[−0.116, +0.157]
Humidity +5 pp, total (μg/m³)	−0.0882	[−0.198, +0.034]	[−0.197, +0.027]	[−0.211, +0.041]

Quantity	Estimate	95% CI (7-day)	95% CI (14-day)	95% CI (30-day)
Humidity +5 pp, instantaneous (μg/m³)	+0.0432	[−0.021, +0.102]	[−0.021, +0.112]	[−0.034, +0.117]
Humidity +5 pp, antecedent (μg/m³)	−0.1314	[−0.240, −0.012]	[−0.246, −0.013]	[−0.254, −0.012]
Wind +10%, total (μg/m³)	−0.1033	[−0.173, −0.040]	[−0.181, −0.041]	[−0.182, −0.039]
Wind +10%, instantaneous (μg/m³)	+0.0024	[−0.017, +0.018]	[−0.018, +0.022]	[−0.020, +0.024]
Wind +10%, antecedent (μg/m³)	−0.1057	[−0.172, −0.048]	[−0.178, −0.045]	[−0.175, −0.047]
Precipitation +10%, total (μg/m³)	−0.0321	[−0.042, −0.020]	[−0.043, −0.020]	[−0.044, −0.019]
Precipitation +10%, instantaneous (μg/m³)	−0.0071	[−0.010, −0.004]	[−0.010, −0.004]	[−0.011, −0.004]
Precipitation +10%, antecedent (μg/m³)	−0.0250	[−0.035, −0.013]	[−0.035, −0.013]	[−0.038, −0.012]

Intervals are 2.5–97.5 percentiles from 1,000 block-bootstrap replicates; point estimates are identical across block lengths. 30-day blocks widen intervals by 3–45%; the antecedent temperature contrast is the only quantity whose interval then includes zero, and all other zero-exclusion and perturbation statements are unchanged. Because residual autocorrelation is 0.275 at 168 h, seven-day intervals are reported as primary with 14- and 30-day intervals alongside.

Table S9: Partial ERA5-Land sensitivity (temperature and relative humidity only)

Quantity	ERA5 (primary)	ERA5-Land partial
2025 hourly RMSE (μg/m³)	5.35	5.40
2025 hourly MAE (μg/m³)	3.16	3.19
2025 hourly MBE (μg/m³)	−0.60	−0.60
2025 hourly R^2	0.421	0.410
2025 daily RMSE (μg/m³)	2.80	2.85
2025 daily R^2	0.598	0.585
Temperature, current hour (%)	−0.5	+12.2
Humidity, current hour (%)	+5.5	+7.5
Wind, current hour (%)	−0.2	−1.1
Precipitation, current hour (%; positive-precipitation-hour p10–p90)	−10.1	−8.6
Temperature, 24-h antecedent (%)	+35.7	+22.8
Humidity, 24-h antecedent (%)	−11.6	−15.5
Wind, 24-h antecedent (%)	−9.1	−9.6
Precipitation, 24-h antecedent (%; positive preceding-24-h totals, p10–p90)	−13.5	−9.6

ERA5-Land provides temperature and relative humidity only for this point in the Open-Meteo archive; ERA5 wind speed and precipitation are retained, so the comparison isolates the effect of the near-surface temperature and humidity product. Training sample, spline specification and λ are unchanged. Contrasts are 10th–90th percentile relative changes in C+1 (%). Both precipitation rows use positive-hour definitions: the current-hour row uses the 10th–90th percentiles of positive-precipitation hours (0.10 to 0.80 mm) and the 24-h antecedent row the 10th–90th percentiles of positive preceding-24-h precipitation totals (0.2 to 7.2 mm); both columns of each row use the same definition. Section 3.3 and Table S8 report a different, explicitly labelled contrast for the current hour (wet-hour 25th–75th percentiles, 0.10 to 0.40 mm), so the two precipitation contrast sets are not expected to coincide.

Table S10: Sensitivity to a ±1 h shift of the meteorological series

Meteorological shift	2025 n	Hourly RMSE	Hourly R^2	Daily RMSE	Temperature, 24-h antecedent (%)	Relative humidity, 24-h antecedent (%)	Wind speed, 24-h antecedent (%)	Precipitation, 24-h antecedent (%)
−1 h	8450	5.342	0.422	2.813	+39.6	−11.8	−10.1	−14.6
+0 h	8451	5.350	0.421	2.802	+35.7	−11.6	−9.1	−13.5
+1 h	8450	5.373	0.415	2.801	+30.3	−12.0	−8.2	−12.9

The entire meteorological series is shifted by one hour in either direction and the model is refitted with the same spline specification and λ; the reported contrasts are 10th–90th percentile relative changes in C+1. The small change in n reflects the shifted antecedent window at the start of 2025.

Table S11: Paired comparison of the primary and boundary-layer-height-augmented models on hours with valid ERA5 boundary-layer height

Model	Training hours	In-sample RMSE (μg/m³)	In-sample R^2	2025 hours	2025 hourly RMSE (μg/m³)	2025 hourly R^2
Primary model, same-subset refit	47,596	6.266	0.336	8,451	5.456	0.398
Primary + boundary-layer height	47,596	6.233	0.343	8,451	5.382	0.414

Both models were refitted with the same knots, λ and retransformation handling on the 47,596 training hours with valid ERA5 boundary-layer height, and evaluated on the same 8,451 paired hours in 2025. The primary row is therefore a same-subset refit, not the full-sample frozen model (2025 hourly RMSE 5.35 μg/m³); the comparison is conditional on this subsample and does not by itself establish improved global predictive skill. Residuals by boundary-layer-height quintile and wind sector are reported in Tables S2 and S3.

Table S12: Analysis stages, software environments, random seeds and retained artifacts

Stage	Environment	Random seed(s)	Computation / retained artifact
Historical model and benchmark fitting (2019–2024)	B	20261013	Fitted spline state and archived 2025 predictions; random forest trained here (archive only)
Frozen-model verification and conditional contrasts	A	20261013	Model rebuilt from the frozen spline state; nine contrasts recomputed from frozen coefficients
Coefficient block-bootstrap intervals (7-, 14- and 30-day)	Historical archive (7- and 30-day arrays); A (14-day array; interval recomputation and checks)	20261013	1,000 replicates per block length; 7- and 30-day archived arrays retained (their A-environment recomputation was used only as a check); 14-day array generated in A; intervals recomputed without refitting
Trend-specification normalization	A	20261014 (SEED+1); 200 draws per month–hour stratum	Retained sampling indices (full digest in the validation package manifest)
Gutor-evening and control-window analysis	A	20261029 (5,000 event-year resamples)	Window statistics, intervals and exact sign test
Losar and Spring Festival day resampling	A	20261030 (5,000 day resamples)	Clean-window excess and intervals
Figure 7 calibration block bootstrap	A	20261030 (1,000 resamples; 7- and 14-day calendar blocks)	Calibration intervals from archived 2025 paired predictions; no coefficient resampling

Environment A is the analysis environment used for the frozen-model verification and the supplementary recomputations reported in this study: Python 3.13.5, NumPy 2.1.3, pandas 2.2.3, SciPy 1.15.3, scikit-learn 1.6.1. Environment B is the historical analysis environment recorded for provenance only: Python 3.12.14, NumPy 2.3.5, pandas 3.0.1, SciPy 1.18.1, scikit-learn 1.9.1; the frozen model state was rebuilt from the archived spline state in environment A because the archived fit object could not be deserialized, and the random forest was not retrained. The 7- and 30-day coefficient arrays used here were retained from the historical analysis archive; the 14-day array was generated in environment A. The 7- and 30-day calculations were independently checked in environment A, but the archived arrays were retained. Interval summaries are recomputed from these arrays without rerunning the coefficient bootstrap in the validation package. The trend-specification normalization stream is fixed at 20261014 (SEED+1) with 200 draws over 288 month–hour strata; the alternative stream (20261013) shifts annual normalized means by at most 0.024 μg/m³. The fixed configuration selects no seed variant at run time. Stage-specific artifacts and file-level hashes are listed in the validation package manifest and provenance note.

Appendix B. Supplementary methods

The following implementation details are provided for reproducibility.

Timestamps are in China Standard Time (UTC+8) and series are matched on their original hourly labels; the QuotSoft archive does not document whether hour H denotes H−1–H or H–H+1, so the hour field is treated as the local hourly mean at hour H. A diurnal audit supports local-time alignment (2 m temperature peaks at 16–17 CST, relative-humidity minimum at 17 CST). Temperature, humidity and 10 m wind speed are instantaneous hourly values; precipitation is preceding-hour accumulation. Zero precipitation and missing values are treated separately. Shifting the weather series by ±1 h changes the 2025 hourly RMSE by at most 0.023 μg/m³ (5.342–5.373 μg/m³) and leaves the signs of all four antecedent contrasts unchanged (Table S10).

Preprocessing checks timestamp uniqueness, hourly continuity and admissible ranges: $PM_{2.5}$ finite and nonnegative, relative humidity 0–100%, wind and precipitation nonnegative. High concentrations are retained, missing concentrations are neither interpolated nor zero-filled; daily evaluation requires at least 18 paired hours and monthly means 75% of expected hours. The fitting period has 2,171 days with at least 18 valid hours; the only fully missing calendar day is 24 August 2019.

Observations are divided into 314 consecutive seven-day blocks (the last containing a single day) with 1,000 block-resampling replicates; 14- and 30-day blocks are reported as sensitivity (Table S8). Pointwise 95% intervals for instantaneous associations and perturbation effects re-estimate coefficients with knots and λ fixed; the retransformation factor is fixed for perturbation intervals. Curves use median references for temperature, humidity and wind; the current-hour precipitation curve uses a dry-hour reference that includes the wet-hour indicator, whereas the 24-hour antecedent precipitation curve uses a zero-total reference (0 mm). All curves express relative changes in C+1. These intervals exclude model-selection, omitted-variable and data-product uncertainty; because autocorrelation persists at long lags, trend intervals were recomputed with 1,000 seven-day and 1,000 thirty-day blocks.

Figure 7 uses a separate calibration resampling that must not be confused with the coefficient bootstrap described above. The 2025 paired predictions are placed on the complete 8,760-hour calendar axis, with the 309 missing hours retained (not interpolated or compressed), leaving 8,451 paired hours. Calendar blocks are contiguous 7-day blocks (53 blocks; the final block contains 24 h) or, as a sensitivity, 14-day blocks (27 blocks; the final block contains 24 h); 1,000 block resamples are drawn for each block length with seed 20261030. The frozen model and the fixed predicted-decile limits are held fixed, so no model is retrained and no coefficient is resampled; the intervals describe the calibration of the saved predictions only. Interval bounds are provided in results/calibration_2025_block_bootstrap.csv of the validation package.

The random forest's +1.24 μg/m³ level bias also stems from its calendar inputs: in-sample MBE is +0.01, but the linear year term is its third most important feature (10.5% impurity importance) after the annual and diurnal harmonics. Removing it reduces the 2025 bias to +0.42 μg/m³, and fitting on the log scale gives −0.17. Block-bootstrap 95% intervals (1,000 seven-day replicates) are −0.12 (−0.20 to −0.04) μg/m³ for additive-minus-linear hourly RMSE and +0.57 (−0.01 to +1.09) for additive-minus-random-forest; the MAE difference relative to the random forest is −0.23 (−0.53 to +0.05). The additive model's advantage over the linear benchmark is robust, whereas the random forest's lower hourly RMSE is not distinguishable from zero once serial dependence is accounted for.